

# Design and off-design performance comparison of supercritical carbon dioxide Brayton cycles for particle-based high temperature concentrating solar power plants

Rui Chen<sup>a,b</sup>, Manuel Romero<sup>b,\*</sup>, Jose González-Aguilar<sup>b</sup>, Francesco Rovense<sup>b,c</sup>, Zhenghua Rao<sup>a</sup>, Shengming Liao<sup>a,\*</sup>

<sup>a</sup> School of Energy and Engineering, Central South University, 410083 Changsha, Hunan, China

<sup>b</sup> High Temperature Processes Unit, IMDEA Energy, Avda Ramón de La Sagra, 3, 28935 Móstoles, Madrid, Spain

<sup>c</sup> University Rey Juan Carlos, Calle Tulipán, 28933 Móstoles, Madrid, Spain

## ARTICLE INFO

### Keywords:

Concentrating solar power  
Supercritical carbon dioxide  
Brayton cycle  
Off-design performance  
Solar particle receiver  
Dry cooling

## ABSTRACT

Concentrated solar power (CSP) plants using dense particle suspension as heat transfer fluid and particles as the storage medium are considered as a promising solution to provide the high temperature required for the supercritical carbon dioxide (S-CO<sub>2</sub>) Brayton cycle. During plant operation, variations in the heat transfer fluid temperature and ambient temperature would significantly affect system performance. Determining the suitable S-CO<sub>2</sub> Brayton cycle configuration for this particle-based CSP plant requires accurate prediction and comprehensive comparison on the system performance both at design and off-design conditions. This study presents a common methodology to homogeneously assess the plant performance for six 10 MW S-CO<sub>2</sub> Brayton cycles (i.e. simple regeneration, recompression, precompression, intercooling, partial cooling and split expansion) integrated with a hot particles thermal energy storage and a dry cooling system. This methodology includes both design and off-design detailed models based on the characteristic curves of all components. The optimal design for each thermodynamic cycle has been determined under the same boundary design constrains by a genetic algorithm. Then, their off-design performances have been quantitatively compared under varying particle inlet temperature and ambient temperature, in terms of cycle efficiency, net power output and specific work. Results show that the variation in ambient temperature contributes to a greater influence on the cycle off-design performance than typical variations of the heat transfer fluid temperature. Cycles with higher complexity have larger performance deterioration when the ambient temperature increases, though they could present higher peak efficiency and specific work at design-point. In particular, the cycle with maximum efficiency or specific work presents significant changes in different ranges of ambient temperature. This means that for the selection of the best configuration, the typical off-design operation conditions should be considered as well. For integrating with high-temperature CSP plants and dry cooling systems, the simple regeneration and the recompression cycles are the most suitable S-CO<sub>2</sub> Brayton cycle configurations due to their fewer performance degradations at ambient temperatures above 30 °C, which is a frequent environmental condition in sunny areas of the world.

## 1. Introduction

Concentrating solar power (CSP) is a reliable and dispatchable technology for the utilization of solar energy, with more than 6 GW installed and grid-connected worldwide by 2020 [1]. Due to the maturity of the conventional steam-Rankine cycle in terms of design and operation, the CSP power block has limited potential for cost reduction and performance improvement. However, it represents typically about

1/3 of the capital expenditure (CAPEX) and it is the system with the highest impact on the conversion efficiency of the CSP plant [2], therefore the implementation of alternative power cycles is a key and necessary development within CSP technology [3]. Supercritical Carbon Dioxide (S-CO<sub>2</sub>) Brayton cycle is anticipated to have smaller turbomachinery weight and volume, lower thermal mass, less complexity and greater cost savings versus Rankine cycles due to the higher fluid density and simpler cycle design [4]. Higher efficiencies are possible because CO<sub>2</sub> can withstand high temperatures without degradation, and requires

\* Corresponding authors.

E-mail addresses: [manuel.romero@imdea.org](mailto:manuel.romero@imdea.org) (M. Romero), [smliao@csu.edu.cn](mailto:smliao@csu.edu.cn) (S. Liao).

<https://doi.org/10.1016/j.enconman.2021.113870>

Received 28 October 2020; Accepted 17 January 2021

Available online 6 February 2021

0196-8904/© 2021 The Authors. Published by Elsevier Ltd. This is an open access article under the CC BY license (<http://creativecommons.org/licenses/by/4.0/>).

Nomenclature	
<i>Acronyms</i>	
CIT	Compressor inlet temperature
CSP	Concentrating solar power
DNI	Direct normal irradiance
DPS	Dense particle suspension
HTF	Heat transfer fluid
HTR	High temperature recuperator
LCOE	Levelized cost of electricity
LTR	Low temperature recuperator
MCIT	Main compressor inlet temperature
MCIP	Main compressor inlet pressure
MCOP	Main compressor outlet pressure
PCHE	Printed circuit heat exchanger
PCIT	Precompressor inlet temperature
PCOP	Precompressor outlet pressure
PHE	Primary heat exchangers
PR	Pressure ratio
RF	Recompression fraction
S-CO <sub>2</sub>	Supercritical carbon dioxide
SPT	Solar power tower
TES	Thermal energy storage
TIP	Turbine inlet pressure
TIT	Turbine inlet temperature
UA	Production of overall heat transfer coefficient and area
UBFB	Bubbling fluidized bed
<i>Latin Letters</i>	
$\dot{Q}$	Heat transfer rate
$\dot{m}$	Mass flow rate
$C$	Capacity rate
$C_p$	Specific heat capacity
$d$	Hydraulic diameter
$f$	Friction
$h$	Specific enthalpy
$k$	Overall heat transfer coefficient; thermal conductivity
$l$	Length of PCHE channel
$N$	Shaft speed
$Nu$	Nusselt number
$Pr$	Prandtl number
$Q$	Heat transfer
$Re$	Reynolds number
$T$	Temperature
$U$	Tip speed of rotor
$u$	Velocity
$W$	Power output
$w$	Specific work
<i>Greek Letters</i>	
$\Delta$	Variation in
$\varepsilon$	Recuperator efficiency
$\zeta_p$	Pressure drop factor
$\eta$	Cycle/turbomachinery efficiency
$\mu$	Dynamic viscosity
$\rho$	Density
$\phi$	Flow coefficient
$\psi$	Ideal head coefficient
$\beta$	Modified heat transfer coefficient
<i>Subscripts</i>	
<i>Air</i>	Air inlet in the dry cooler
<i>areo</i>	Aerodynamic process
<i>c</i>	Compressor; cold
<i>cycle</i>	Cycle design
<i>h</i>	Hot
<i>i</i>	i-th element
<i>in</i>	Inlet
<i>ise</i>	Isentropic process
<i>max</i>	Maximum
<i>min</i>	Min
<i>net</i>	Net value
<i>out</i>	Outlet
<i>t</i>	Turbine
<i>DPS</i>	DPS inlet in the primary heat exchanger

less compression work close to the critical point [5]. Besides, the flexible heat rejection strategy is another attractive characteristic of the S-CO<sub>2</sub> Brayton cycle. CO<sub>2</sub> has a nearly ambient critical temperature (31.2 °C), allowing the dry cooling technology to be incorporated making it especially suitable for use in arid regions with abundant solar resources and water scarcity [6].

Despite its simplicity, it is a highly regenerative cycle subject to a variety of solutions of internal heat management involving significant heat exchangers between fluids with dissimilar thermal properties and flowrates. Various configurations of the S-CO<sub>2</sub> Brayton cycle have been proposed in the literature based on the original proposals of Angelino and Feher [7]. To improve system thermo-economic performance, Dostal [6] proposed five configurations of the S-CO<sub>2</sub> Brayton cycle, including simple recuperation, recompression, precompression, reheating, and partial-cooling cycle by adding additional compressors and recuperators. The recompression cycle has been recommended for properly solving the pinch-point problem with high efficiency [8]. Derived from recompression cycle, Turchi *et al.* [4] found that the recompression cycle with intercooling could achieve greater than 50% efficiency with dry cooling, though it is highly dependent on the ambient temperature at the site. Ruiz-Casanova *et al.* [9] recommended adopting the intercooled recuperated Brayton cycle in low-grade geothermal heat sources for its high electric power output, energy and exergy efficiencies. Guo *et al.* [10] comprehensively compared the

energy, exergy and economic performances of three S-CO<sub>2</sub> power cycles integrated with an optimized coal boiler layout. In addition to the conventional exergy analysis, Liu *et al.* [11] also conducted an advanced exergy analysis considering the interactions among components and technological limitations to further reveal the pragmatic potential for system performance improvements. Crespi *et al.* [12] reviewed forty-two stand-alone S-CO<sub>2</sub> power cycles and thirty-eight combined layouts with potential use in different industry areas and investigated the thermo-economic performance of partial-cooling cycle for eventual integration in Solar Power Tower (SPT) systems with different turbine inlet temperature (TIT) and pressure ratio (PR) [13].

Besides investigating the power cycle independent from the energy source, many studies have focused on the steady-state modelling of the S-CO<sub>2</sub> Brayton cycle integrated with SPT system. Several optimization approaches have been proposed to find the optimal design conditions and appropriate cycle configurations. There are mainly two approaches for the integration: direct integration and indirect integration. In the direct integration, the S-CO<sub>2</sub> is used as both the working fluid in power cycle and the heat transfer fluid in the solar receiver, which could contribute to a higher receiver outlet temperature and fewer system components. Al-Sulaiman and Atif [14] compared the thermodynamic performance of five S-CO<sub>2</sub> Brayton cycles directly integrated with a SPT system, including the simple cycle, regenerative cycle, recompression, precompression and split expansion cycle. They found that the

recompression cycle reached the highest cycle efficiency at solar noon, while the simple regenerative cycle performed better during low direct normal irradiance (DNI) periods. Furthermore, Zhu *et al.* [15] found that the intercooling cycle could achieve higher cycle efficiency and the partial-cooling cycle could provide higher specific work than the recompression cycle. Although the S-CO<sub>2</sub> Brayton cycle appeared manageable under part heat load operation for short durations [16], there are still many technical restrictions in the S-CO<sub>2</sub> solar receiver design, materials and control strategy development. Instead, the indirect integrated system can be more easily realized by adopting the concept of two-tank molten salt. Wang *et al.* [17] compared the performance of six S-CO<sub>2</sub> Brayton cycle layouts integrated with molten salt thermal energy storage (TES) and the solar tower system. Results indicated that the intercooling cycle could generally offer the highest efficiency, followed by the partial-cooling cycle and the recompression cycle. They also conducted a multi-objective optimization for these cycles based on simultaneously considering the cycle efficiency and specific work [18]. Ma *et al.* [19] performed an exergo-economic comparison between the reheating and no-reheating S-CO<sub>2</sub> intercooling Brayton cycle integrated with molten salt solar power plant and then optimized six crucial variables with the objective of minimal total unit exergy cost. Neises and Turchi [20] investigated the performance and cost trade-offs of three S-CO<sub>2</sub> Brayton cycles integrated with a molten salt SPT system under different recuperator conductances. It was found that the partial-cooling cycle had the largest temperature range of heat input, leading to cheaper two-tank TES, higher receiver efficiencies, and lower mass flow rates in the power tower, and thus less minimum levelized cost of electricity (LCOE) than the simple cycle and the recompression cycle.

Despite the mature technologies in thermal energy storage and efficient receiver design for molten salts, further efficiency improvements are constrained by their relatively low degradation temperature (about 600 °C). Particle solar receiver is considered as an attractive technology pathway with the potential to deliver the high temperatures (>700 °C) required by S-CO<sub>2</sub> Brayton cycle [3,19]. Up bubbling fluidized bed (UBFB) indirectly irradiated solar particle receivers with a novel heat transfer fluid (HTF) based on a dense particle suspension (DPS) consisting of very small particles, such as silicon carbide or olivine with mean particle size  $d_{50} = 59 \mu\text{m}$  and density = 3300 kg/m<sup>3</sup>, which can be easily fluidized at low gas velocities and stored economically. Reyes-Belmonte *et al.* [21] optimized the integration of recompression S-CO<sub>2</sub> cycle with a DPS central receiver CSP plant and observed a near 50% net cycle efficiency. The feasibility of annual operation of subcritical steam Rankine cycle coupled to the particle receiver solar power plant was also demonstrated by the authors though with lower conversion efficiencies [22].

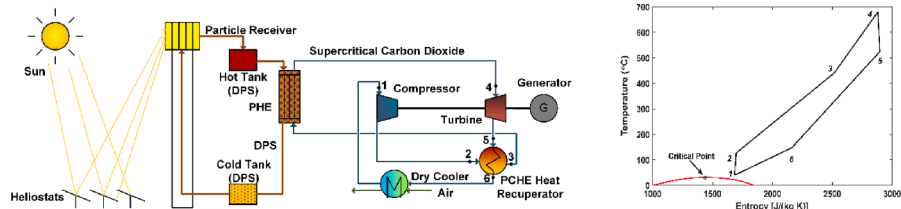
The integration of TES could mitigate transient perturbations of DNI fluctuations though, the S-CO<sub>2</sub> Brayton cycle with DPS solar system might operate under off-design or part-load conditions as well. When the plant operates in load-following mode, the power cycle output is required to augment or decrease in response to grid power demand. Depending on the operation and control or dispatch strategies employed, and for specific solar receiver load conditions or DNI fluctuations, the power cycle might need to operate at varying DPS temperature. Furthermore, if the S-CO<sub>2</sub> cycle uses the dry cooling system, the dramatic variation of ambient temperature in sunny areas with high DNI will directly influence compressor inlet temperature, which is a key parameter for the whole cycle performance. Therefore, accurate prediction for the system off-design performance is decisive for the utilization of the S-CO<sub>2</sub> power cycle used in SPT systems.

Dyreby *et al.* [23] developed the off-design models of S-CO<sub>2</sub> recuperation and recompression cycle and examined the cycle performance at higher off-design compressor inlet temperatures (CIT) and lower TITs. Their semiempirical models of turbomachinery, which were obtained by extrapolating the experimental data from laboratory-scale S-CO<sub>2</sub> turbomachinery to large-scale power cycles, have been widely adopted by other authors [24–29]. To further accommodate real components

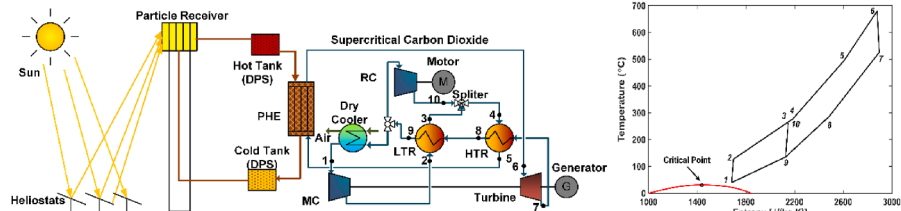
design and changes in fluid thermophysical properties, Saeed *et al.* [30] established a mean line model of turbomachinery along with a one-dimensional steady-state model for heat exchangers. De la Calle *et al.* [24] investigated the impact of ambient temperature on the off-design performance of a S-CO<sub>2</sub> recompression cycle with dry cooling. They also extrapolated a series of polynomial regressions for the net power output drop and used them to simulate the annual system performance. Instead of using constant minimum temperature difference in the cooler like Ref. [24], Duniyam and Veeraragavan [25] introduced a detailed model of natural draft dry cooling tower into the whole off-design model. They found that the cycle could maintain nominal net power generation at 50 °C ambient temperature with increased cycle mass flow rate and TIT. Neises [31] demonstrated that compressor shaft speeds control could improve the performance of the recompression S-CO<sub>2</sub> Brayton cycle when the ambient temperature or HTF mass flow is below its design value. Wang *et al.* [27] analyzed a parabolic trough solar power plant integrated with a direct air-cooled S-CO<sub>2</sub> recompression Brayton cycle and investigated the impacts of PR, recompression fraction (RF), shaft speed, ambient temperature and solar intensity on the power output. Yang *et al.* [28] studied the off-design performance of the system integrated with a simple recuperated S-CO<sub>2</sub> Brayton cycle, solar tower and molten salt TES. They assumed the system was hybrid and backed-up with biomass when the DNI was insufficient and thus the TIT was constant. Instead of focusing on the off-design performance of S-CO<sub>2</sub>, they assessed more in detail the effect of ambient temperature and solar power input on the receiver efficiency. Furthermore, the authors [29] compared the part-load performance of four S-CO<sub>2</sub> Brayton cycles including the simple regeneration, reheating, recompression and intercooling cycle. They adjusted the system maximum and minimum pressure and RF to follow the changing power output demand by assuming constant TIT and CIT.

The main objective of this study is to develop a harmonized methodology to investigate both the design and off-design performance of the dry-cooling S-CO<sub>2</sub> Brayton cycles for particle central receiver CSP plants. In particular, the proposed methodology can be used to evaluate the effect of particle inlet temperature and ambient temperature variations on the performance of different systems and thus to identify the most efficient thermodynamic cycles. Using hot particles as the storage medium in TES is a promising way to achieve the development goals in the Gen3 Roadmap [3], while most previous studies have only investigated systems coupled to molten salt TES system [15,23,25,26]. Quantitative analysis and comprehensive comparison for the off-design performance of different S-CO<sub>2</sub> Brayton cycles are required to identify the optimal configuration integrated with particles-based thermal storage, not only regarding the system design performance but also the annual operation. Although some efforts have been made to investigate the off-design performance of simple and recompression S-CO<sub>2</sub> Brayton cycle at different heat and cold sources temperature, the off-design performance of more complex cycle layouts, including pre-compression, intercooling, partial cooling and split expansion cycle, remains unclear. Previous studies mostly considered the dry cooler performance with a constant TIT [22,23] or investigated the part-load performance with a constant CIT [29], the detailed influence mechanism among the operational parameters of turbomachinery and heat exchangers is still uncertain, especially for complex configurations. Studies are still needed to investigate the effect of performance improvement technical solutions, for instance adding recuperators, recompression and intercooling, on the system performance under off-design conditions, such as lower DPS temperature or higher ambient temperature.

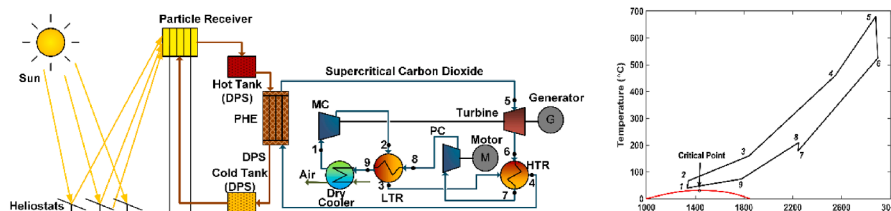
In this study, a common methodology has been developed with detailed design and off-design thermodynamic models of six typical 10 MW S-CO<sub>2</sub> Brayton cycles integrated with a two-tank particle TES system fed by a DPS solar receiver and with a dry cooling system. The investigated configurations include the simple regeneration, recompression, precompression, intercooling, partial cooling and split



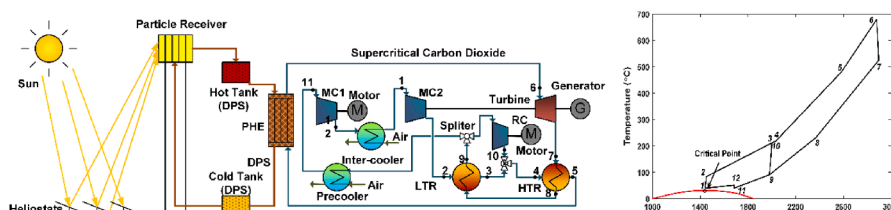
(a) Simple regeneration S-CO<sub>2</sub> Brayton cycle and corresponding T-s diagram.



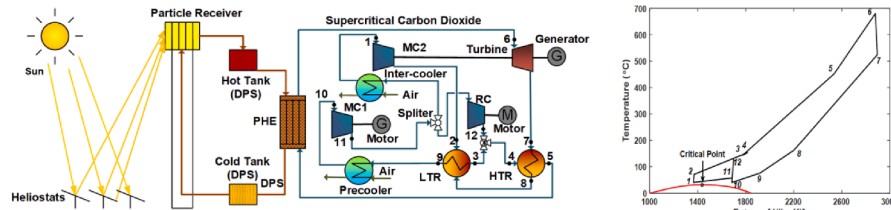
(b) Recompression S-CO<sub>2</sub> Brayton cycle and corresponding T-s diagram.



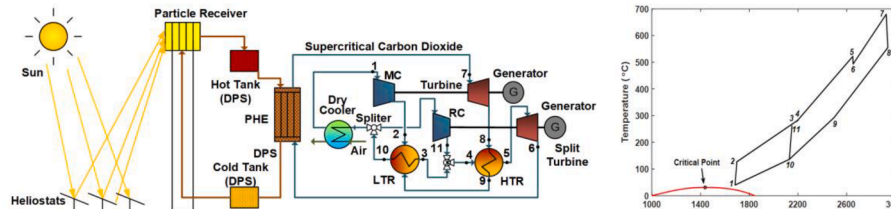
(c) Precompression S-CO<sub>2</sub> Brayton cycle and corresponding T-s diagram.



(d) Intercooling S-CO<sub>2</sub> Brayton cycle and corresponding T-s diagram.



(e) Partial cooling S-CO<sub>2</sub> Brayton cycle and corresponding T-s diagram.



(f) Split expansion S-CO<sub>2</sub> Brayton cycle and corresponding T-s diagram.

Fig. 1. Schematic diagrams for six S-CO<sub>2</sub> Brayton cycle integrated with dense particle receiver and their corresponding T-s diagrams. MC, MC1, and MC2 refer to the main compressor, main compressor 1 and main compressor 2 respectively; RC refers to recompressor; PHE refers to the primary heat exchanger; HTR and LTR refer to high and low temperature recuperator respectively.

expansion cycle. In design point, same boundary conditions and components efficiency have been used and critical design parameters (RF, intermediate pressure for precompression, and intermediate pressure for split expansion) have been optimized by genetic algorithms to achieve maximum cycle efficiency. The preliminary component design has been made to get the geometric parameters used in semi-empirical off-design models of turbomachinery and coefficient correlations of heat exchangers. The off-design performance of six configurations has been then quantitatively assessed when the DPS inlet temperature and ambient temperature differ from the design values. Both design and off-design performance of these six configurations have been compared in terms of three aspects, i.e., cycle efficiency, net power output and specific work. Results can guide for selecting the S-CO<sub>2</sub> Brayton cycle with superior operating performance after coupling the particle central receiver SPT plants and dry-cooling system.

## 2. System configurations description

Solar power plants using particle receiver concept coupled with six common S-CO<sub>2</sub> Brayton cycles are shown in Fig. 1(a)–(f), respectively. These plants consist of the heliostat field, the solar particle receiver using DPS as HTF, two storage tanks and the power block with S-CO<sub>2</sub> Brayton cycle devices. During the operation, DPS is directly heated by concentrated sunlight inside the tubular panel of the solar receiver and stored in an insulated tank. Then the high-temperature particles transfer the heat to the S-CO<sub>2</sub> in the primary heat exchanger (PHE). Silicon Carbide particles have been considered for the solar loop as the reference case. The introduction of storage tank thermally decouples the solar loop and power cycle, hence the variation of solar thermal heat input in the cycle can be represented by the mass flow rate and outlet temperature of DPS from the hot tank. Therefore, the system modelling in this paper focuses on the power block with suitable assumptions regarding the interface with the DPS solar power plant. The investigated S-CO<sub>2</sub> Brayton cycles in this paper include the simple regeneration, the recompression, the intercooling, the partial-cooling and the split expansion cycles. These six cycles consist of similar components, i.e. compressors, turbines and heat exchangers, while they present different component arrangements.

### 2.1. Simple regeneration cycle

Fig. 1(a) shows the configuration and corresponding T-s diagram of simple regeneration S-CO<sub>2</sub> Brayton cycle, which incorporates a recuperator in the original Brayton cycle to recover the waste heat. Since the heat regeneration is generally required, the simple regeneration, instead of the original cycle, is always considered as the reference layout, and more sophisticated layouts can be derived from it [32]. In this cycle, state 1 corresponds to the compressor inlet, which is near the CO<sub>2</sub> critical point. In the compressor, the S-CO<sub>2</sub> is compressed to high pressure (point 1 to 2) and preheated in the printed circuit heat exchanger (PCHE) recuperator to state 3. Then the S-CO<sub>2</sub> is heated to the maximum temperature by particles in the PHE. From the PHE, the high-temperature and high-pressure S-CO<sub>2</sub> (state 4) expand in the turbine to transform the fluid energy into rotational work of shaft which connects the compressor, turbine and generator. The exhaust fluid (state 5) is subsequently cooled down in the recuperator (state 6) and dry air cooler, where the compressor inlet temperature is reached by rejecting energy to the ambient.

### 2.2. Recompression cycle

Though the introduction of recuperator recovers much waste heat, the cycle efficiency is still limited by the pinch-point problem, which means that the temperature difference at some points may be smaller than the minimum temperature difference [21]. This is caused by specific S-CO<sub>2</sub> thermo-physical properties. In the low-temperature part of

the recuperator, the specific heat in the cold stream is nearly two times greater than that in the hot stream. To solve the pinch-point problem, the recompression cycle is proposed by decreasing the mass flow rate of the high-pressure stream [7]. Compared to the simple regeneration cycle, the recompression cycle adds an additional compressor (recompressor) and splits the low-pressure stream by dividing the regenerator into two parts: the low temperature recuperator (LTR) and the high temperature recuperator (HTR) as shown in Fig. 1(b).

### 2.3. Precompression system

Precompression cycle is another alternative configuration to reduce the pinch-point problem by increasing the pressure of the low-pressure stream. Instead of splitting the CO<sub>2</sub> mass flow rate, the precompression cycle introduces an additional compressor (i.e. pre-compressor) between the HTR and LTR, as shown in Fig. 1(c). Before entering the LTR, the S-CO<sub>2</sub> flows in the outlet of HTR (state 7) and is compressed by precompressor to state 8. The introduction of pre-compressor also decouples the main compressor inlet pressure from turbine outlet pressure, giving more flexibility in the system optimization.

### 2.4. Intercooling system

To further improve system performance, intercooling is added to the recompression cycle for reducing the compressor work. This arrangement divides the main compression into two stages, which benefits the cycle optimization by decoupling the main compressor inlet temperature and the turbine outlet pressure. According to the location of flow splitting, the possible configurations of recompression cycle with intercooling can be classified into the recompression cycle with main-compression intercooling (intercooling cycle, Fig. 1(d)) and the recompression cycle with precooling (partial cooling cycle, Fig. 1(e)) [4]. Derived from the recompression cycle, the low temperature and pressure stream is compressed by main compressor 1 to the intermediate pressure of state 12. Next, this stream enters the intercooler to be cooled down to the designed inlet temperature of main compressor 2 (state 13). Finally, the stream is further compressed in the main compressor 2 to the designed cycle highest pressure. The inlet temperatures of pre-compression and main compressor can be different in theory, but since both the pre-cooler and intercooler use dry air as cold sink [4], these two temperatures are considered to be the same in this study.

### 2.5. Partial cooling system

Partial cooling cycle is another way to introduce multistage compression with intercooling in the recompression cycle to improve system efficiency. The power cycle block in Fig. 1(e) is the partial cooling S-CO<sub>2</sub> cycle, which refers to the recompression cycle with pre-cooling, as mentioned in the previous section. In this configuration, the mainstream is further cooled by the pre-cooler after exiting from LTR and then is split after the pre-compressor at state 11. A fraction of the stream enters the recompressor, while the remaining is cooled by the inter-cooler to state 1 and compressed in the main compressor to state 2 successively. Because of the precompression procedure, the recompressor operates over a fraction of the turbine pressure ratio. Similar to the intercooling cycle, the inlet temperatures of the pre-compressor (state 10) and the main compressor (state 1) are equal.

### 2.6. Split expansion cycle

To obtain high system performance, the S-CO<sub>2</sub> Brayton cycle always operates in the high pressure and temperature regions, which presents challenges in materials durability and cost, especially in the PHE. Therefore, derived from the recompression cycle, the split expansion cycle introduces an additional turbine between the HTR and the PHE to

reduce the thermal stress. As shown in Fig. 1(f), the high-pressure stream at the outlet of HTR (state 5) expands in the split turbine to state 6 before entering the PHE. In the PHE, the S-CO<sub>2</sub> is heated to maximum temperature (state 7). The remaining S-CO<sub>2</sub> flow path is similar to the recompression cycle.

In the end, the recompression and precompression cycle represent two possible ways to solve the pinch-point problem in the simple regeneration cycle. The intercooling, partial cooling and split expansion cycle are all derived from the recompression cycle, the difference between them being that the intercooling and partial cooling have an additional precompressor and intercooler but in different positions, while the split expansion cycle has an additional split expander.

### 3. Modelling methods

This work is carried out by developing the design and off-design models for each component and then integrating them into a system-level model. All components models, including compressors, turbines, PHE, recuperators and dry-coolers, are based on the mass and energy balances at steady-state. The mathematical models for all six cycles are encoded in MATLAB [33]. The working fluid properties are provided from REFPROP 9.1 [34]. Silicon Carbide particles have been chosen as the working fluid in the solar loop and the material properties are referred to [22].

#### 3.1. Design point modelling

Design point analysis is used to determine the thermodynamic conditions of all the cycle components, including their inlet/outlet states, heat loads or power requirements, which are fundamental for further component geometry design [5]. The main assumptions in the developed thermodynamic models are as follows:

- (1) The kinetic and potential energy changes in DPS, S-CO<sub>2</sub> and air are neglected.
- (2) The energy losses in pipelines, generator, motor and junctions are neglected.
- (3) The pressure drops in the heat exchanger are mainly due to the frictional losses along the channel length, while the entrance loss, exit losses and acceleration effect are neglected.
- (4) The S-CO<sub>2</sub> fluid undergoes an adiabatic but non-isentropic process in compressor and turbine.

##### 3.1.1. Turbine and compressor design modelling

Processes in turbine and compressor at design condition are assumed as adiabatic but non-isentropic with constant isentropic efficiencies. The isentropic efficiency ( $\eta_{ise}$ ) refers to the ratio of the real work done in the process to the work produced in the isentropic process. When the isentropic efficiency is determined, the isentropic specific work ( $w_{ise}$ ) of a turbomachine can be calculated according to:

$$w_{ise} = h_{in} - h_{out,ise} \quad (1)$$

where  $h_{in}$  is the specific enthalpy of S-CO<sub>2</sub> in the turbomachine inlet;  $h_{out,ise}$  refers to the specific isentropic enthalpy of S-CO<sub>2</sub> in the turbomachine outlet, which is calculated according to the designed fluid outlet pressure and inlet specific entropy.

The actual specific power of compressor ( $w_c$ ) and turbine ( $w_t$ ) can be obtained in Eq. (2) and Eq. (3), respectively.

$$w_c = \frac{w_{ise,c}}{\eta_{ise,c}} \quad (2)$$

$$w_t = w_{ise,t} \cdot \eta_{ise,t} \quad (3)$$

The net cycle power without parasitic losses ( $W_{net}$ ) equals the power generated by turbines subtracting the power consumed by compressors.

$$W_{net} = \sum \dot{m}_{CO_2,t} \cdot w_t - \sum \dot{m}_{CO_2,c} \cdot w_c \quad (4)$$

where  $\dot{m}_{CO_2,t}$  and  $\dot{m}_{CO_2,c}$  refer to the mass flow rate going through the turbine and compressor respectively, which will be different according to the cycle layout. For example, the mass flow rate going through the recompressor is the product of the cycle mass flow and RF. The cycle mass flow rate is the value when the  $W_{net}$  equals the specified power output at the design point.

#### 3.1.2. Heat exchanger design modelling

There are mainly three types of heat exchangers used in the S-CO<sub>2</sub> Brayton cycle:

- a) the recuperators are used to recover the heat of the working fluid CO<sub>2</sub> from the hot side to the cold side;
- b) the PHE, where the working fluid CO<sub>2</sub> absorbs heat from high-temperature particles before entering the turbine; and
- c) the precooler that rejects heat of S-CO<sub>2</sub> to the ambient air.

Among all possible heat exchanger designs, PCHE is chosen as appropriate for the S-CO<sub>2</sub> Brayton cycle because of its great compactness and capability to withstand the high temperature and pressure [6]. Compared with straight and zigzag PCHE, S-shaped fin PCHE has better thermal-hydraulic performances: greater heat transfer ability, relatively lower pressure drops and cost [32,33]. Thus, the recuperators have been modelled as S-shaped fin PCHE, which were designed by optimizing simultaneously the whole cycle thermodynamic and economic performances as reported in a previous study [36]. However, since the information on modelling the PCHE used for heat transfer from particles and air to S-CO<sub>2</sub> is limited, the detailed geometry design of PHE and pre-cooler have been simplified in this study. The detailed modelling methods for heat exchanger are shown in Appendix A.

#### 3.2. Off-design condition modelling

Based on the design condition analysis in the previous section, the turbomachinery maps and heat exchanger performance coefficients can be obtained according to the system hardware selections, which enable to predict the cycle off-design performance. Compared to centrifugal turbomachines, radial turbomachines are preferred to attain better performance for a wider range of cycle's off-design operations and more suitable for S-CO<sub>2</sub> power plants with a 0.3–30 MWe capacity [37]. Therefore, the compressor and turbine used in the investigated system capacity (10 MW) are designed as a single-stage radial type. A 3D physics-based model is reported in Ref. [30]; however, it is found that the semi-empirical model developed by Dyreby [38] requires less computation effort and is easier to apply in various cycle configurations. The semi-empirical models are described in the following sections.

##### 3.2.1. Compressor off-design modelling

The compressor off-design model computes the compressor performance and outlet conditions of S-CO<sub>2</sub> from the inlet conditions of S-CO<sub>2</sub> and geometry parameters. Based on the semi-empirical model in Ref. [38], the radial compressor performance can be described by dimensionless flow and ideal head coefficients. The ideal head coefficient ( $\psi$ ) and compressor off-design efficiency ( $\eta_c^*$ ) are both functions of the flow coefficient ( $\phi$ ), and their functional relationships are expressed as:

$$\phi = \frac{\dot{m}_{CO_2,c}}{\rho_{in} U_c D_c^2} \left( \frac{N}{N_{design}} \right)^{1/5} \quad (5)$$

$$\psi = \frac{\Delta h_{ise}}{U_c^2} \left( \frac{N_{design}}{N} \right)^{(20\phi)^3}, \text{ and} \quad (6)$$

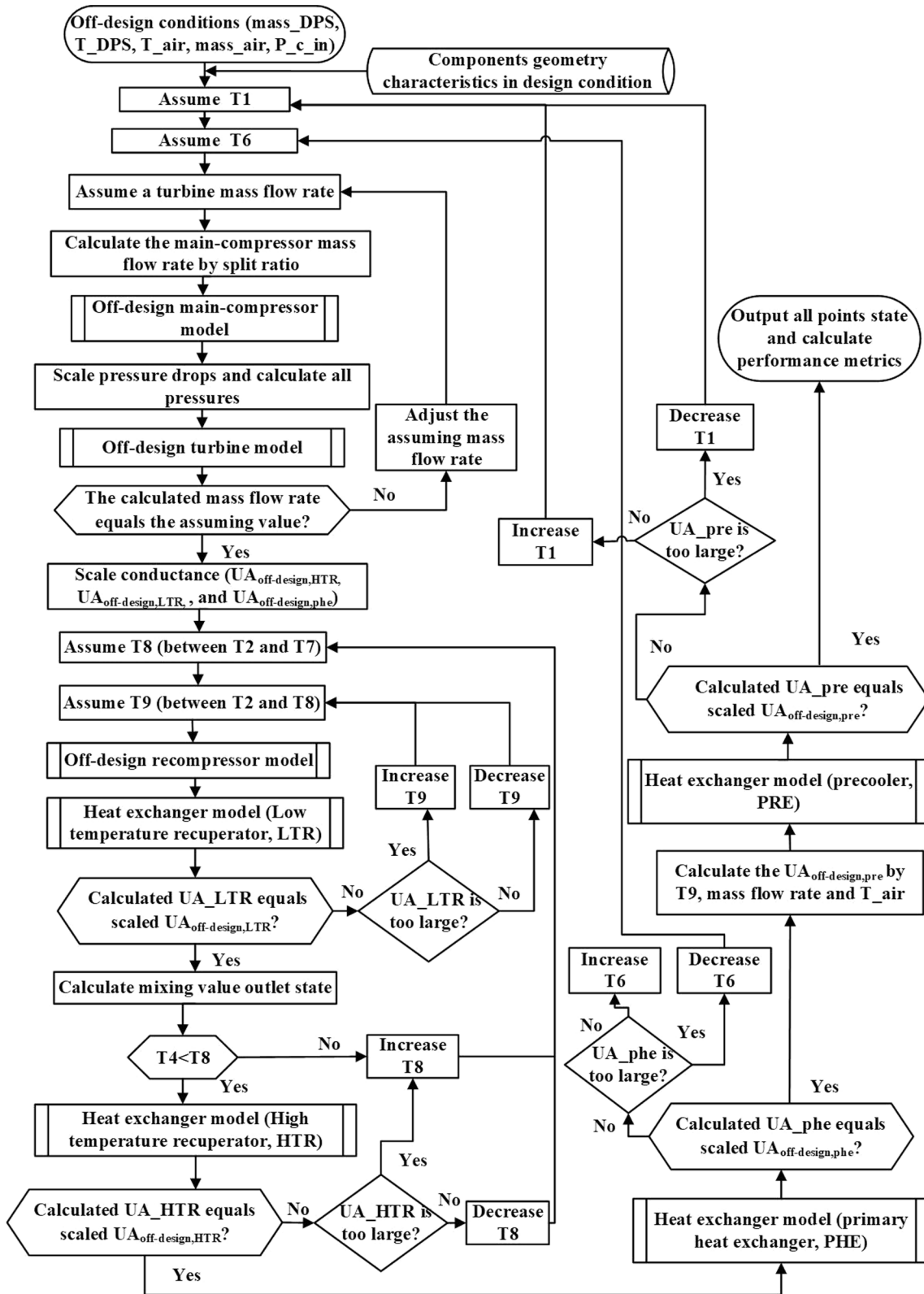


Fig. 2. The off-design performance calculation flowchart of the recompression cycle.

$$\eta_c^* = \eta_{c,design} \left( \frac{N_{design}}{N} \right)^{(20\phi)^3} \quad (7)$$

where  $\rho_{in}$  is the density of S-CO<sub>2</sub> at the compressor inlet;  $U_c$  is the tip speed of the rotor;  $D_c$  is the rotor diameter;  $N$  is the shaft speed;  $N_{design}$  is the design shaft speed and  $\Delta h_{ise}$  is the isentropic enthalpy rise of the S-

CO<sub>2</sub> through the compressor.

Sandia National Laboratories [39] issued one of the most comprehensive compressor physical studies based on experimental data from a 50 kW S-CO<sub>2</sub>, thus the present study deduces indicative performances of compressors in different layouts based on Sandia's prototype. Furthermore, applying the modified definitions shown in Eqs. (5)–(7) to the

experimental data in Ref., the functional relations among the ideal head coefficient, efficiency and flow coefficient can be extrapolated as follows [40]:

$$\psi = -498626\phi^4 + 53224\phi^3 - 2505\phi^2 + 54.6\phi + 0.04049 \quad (8)$$

$$\eta_c^* = -1638000\phi^4 + 182725\phi^3 - 8089\phi^2 + 168.6\phi - 0.7069 \quad (9)$$

When the compressor efficiency at the off-design condition is calculated, the corresponding pressure rises and work consumption can be determined by a similar approach in design analysis. The recompressor off-design model is similar to the compressor off-design model, but its efficiency is determined using the mass flow rate and required outlet pressure (equal to the outlet pressure of the main compressor); the required shaft speed is also calculated in this manner.

### 3.2.2. Turbine off-design modelling

Since the S-CO<sub>2</sub> performs like an ideal-gas in the turbine, the turbine can be modelled based on a general dimensionless approach for radial turbines. This approach assumes the turbine as an adiabatic nozzle [41] and simulates the turbine performance by the following equations. Assuming most of the pressure drop is through the nozzles, the mass flow rate through the turbine is proposed in a first-order approximation [26]:

$$\dot{m}_{co_2} = A_{nozzle} \rho_{out} C_s \quad (10)$$

where  $A_{nozzle}$  is the effective nozzle area of the turbine;  $\rho_{out}$  is the density of S-CO<sub>2</sub> at the turbine outlet and  $C_s$  is the spouting velocity, which is the velocity that will be achieved at the turbine outlet during an isentropic expansion:

$$C_s = \sqrt{2(h_{in} - h_{ise,out})} \quad (11)$$

From Eq. (11), it can be seen that  $\dot{m}_{co_2}$  is strongly dependent on the inlet conditions and geometry design. Once the inlet conditions of turbine change, mainly caused by the heat sink temperature or compressor outlet conditions, the mass flow rate of the whole cycle will be modified and hence the system performance will change.

The turbine off-design efficiency ( $\eta_t^*$ ) is calculated by multiplying the aerodynamic efficiency ( $\eta_{aero}$ , that is the efficiency of an ideal turbine with no internal losses) by the turbine design point efficiency ( $\eta_{t, design}$ ) [38]:

$$\eta_t^* = \eta_{t, design} \eta_{aero} = \eta_{t, design} 2v\sqrt{1-v^2} \quad (12)$$

where  $v$  is the velocity ratio, which is the ratio of rotor tip speed to spouting velocity. The rotor tip speed of the turbine is the same as that of the corresponding connected compressor according to the cycle layout. The relationship between the aerodynamic efficiency ( $\eta_{aero}$ ) and velocity ratio ( $v$ ) shown in Eq. (12) is proposed in Ref. [42]. The turbine efficiency is also further extrapolated as a quartic polynomial from the experimental data of a S-CO<sub>2</sub> turbine in Ref. [43]:

$$\eta_{aero} = 1.0626v^4 - 3.0874v^3 + 1.3668v^2 + 1.3567v + 0.17992118 \quad (13)$$

The turbine wheel diameter is determined for getting the maximum turbine efficiency at the designed shaft speed, which is equal to the shaft speed of the connected compressor. For Eq. (12), the maximum efficiency is achieved at a velocity ratio of 0.707 [40]. Once the mass flow rate and efficiency of the turbine are determined, the outlet conditions of S-CO<sub>2</sub> and turbine power output can be obtained according to the similar method in design analysis. The compressor and turbine are connected on the main shaft and the recompressor is placed on a separate shaft driven by an electric motor.

### 3.2.3. Heat exchanger off-design modelling

The off-design performance of heat exchanger is evaluated by scaling conductance and pressure drop with mass flow rate. When the average fluid properties in the heat exchanger do not change significantly in off-

design conditions, thermal conductance ( $UA$ ) and pressure drop scale ( $\Delta P$ ) with mass flow rate from their design-point according to [23]:

$$\frac{UA}{UA_{design}} = \frac{\dot{m}_{h, design}^{-0.8} + \dot{m}_{c, design}^{-0.8}}{\dot{m}_h^{-0.8} + \dot{m}_c^{-0.8}} \quad (14)$$

$$\Delta P = \Delta P_{design} \cdot \left( \frac{\dot{m}}{\dot{m}_{design}} \right)^{7/4} \quad (15)$$

However, when the fluid works near the vicinity of the critical point, the variation of thermodynamic properties at both sides must be taken into account. Thus, the relationship between  $UA$  and  $UA_{design}$  is presented by the modified heat transfer coefficients ( $\beta$ ):

$$\frac{UA}{UA_{design}} = \frac{\beta_h^{-1} + \beta_c^{-1}}{\beta_h^{-1} + \beta_c^{-1}} \quad (16)$$

$$\beta = \dot{m}^{0.8} \cdot C_p^n \cdot k^{(1-n)} \cdot \mu^{(n-0.8)} \quad (17)$$

where  $n = 0.4$  for hot fluid and  $n = 0.3$  for cold fluid;  $C_p$ ,  $k$  and  $\mu$  is the specific heat capacity, thermal conductivity and dynamic viscosity of the stream at each division, respectively.

### 3.2.4. Off-design cycle iteration

The recompression cycle is the most common investigated cycle nowadays and integrates both the recuperation and recompression process. Considering the convenience of model validation, the recompression cycle is selected as an example for explaining the iteration flow chart and model validation. The calculation algorithms for the other five configurations are similar to the flow chart shown in Fig. 2 just by adding, removing or changing the location of some specific processes. Apart from components geometry characteristics at design-point, the off-design mode inputs include the inlet temperature and mass flow rate of DPS and air, as well as the inlet pressure of the main compressor. Specifying these values fully constrains the set of equations derived from energy and mass balances on the components under off-design conditions. Nested iteration strategy has been used to find the numerical solution of the set of equations. There are five iteration loops in total. The outermost iteration loop is initiated by guessing a value for the main compressor inlet temperature ( $T_1$ ). Given a value for  $T_1$ , control moves to the turbine inlet temperature ( $T_6$ ) iteration loop and after the calculation logic moves to the mass flow rate iteration process, which is determined by matching the head-flow curve of the main compressor with the flow characteristic of the turbine. Once the mass flow rate through the cycle has converged, the temperatures at the remaining unknown state points can be determined by the iteration loop of matching the conductance in recuperators. Root-finding algorithms have been used to check the matching between the calculated conductance and scaled conductance from Eqs. (14) and (16).

Performance evaluation criteria used in this paper are the net power output ( $W_{net}$ ), shown in Eq. (4), cycle efficiency ( $\eta_{cycle}$ ), and specific work ( $w$ ). The cycle efficiency is the ratio of net power output to the heat absorbed by S-CO<sub>2</sub> in the primary heat exchanger ( $Q_{PHX}$ ) and specific work is work per unit weight. Thermal input ratio ( $R_{thermal}$ ) is the heat absorbed by S-CO<sub>2</sub> in the PHE at off-design condition ( $Q_{PHX}$ ) divided by its design value ( $Q_{PHX, design}$ ).

$$\eta_{cycle} = \frac{W_{net}}{Q_{PHX}} \quad (18)$$

$$w = \frac{W_{net}}{\dot{m}_{co_2}} \quad (19)$$

$$R_{thermal} = \frac{Q_{PHX}}{Q_{PHE, design}} \quad (20)$$

**Table 1**  
Operation conditions used for the design point model validation. (Cycle layout: Recompression cycle).

Parameters	Dostal [6]	Ishiyama <i>et al.</i> [44]	Dyreby [38]	Note
Compressor inlet temperature (°C)	32	35	45	
Compressor inlet pressure (kPa)	7692	8190	9170	
Turbine inlet temperature (°C)	550	480	700	
Pressure ratio (-)	2.6	2.51	2.73	
Compressor efficiency (%)	89	88.3	89	
Turbine efficiency (%)	90	93.4	93	
HTR efficiency (%)	96.3	97.9	93.11	(UA = 823 kW/K) <sup>a</sup>
LTR efficiency (%)	92.1	96.1	91.85	(UA = 677 kW/K) <sup>a</sup>
Recompression fraction (-)	0.37	0.33	0.221	
Percentage error reference vs calculated (%)	0.08	0.75	0.6	

<sup>a</sup> The heat exchanger effectiveness is calculated based on the UA value presented in Ref. [38].

3.3. Model validation

Validations of the developed power cycles model have been carried out using the recompression cycle as a typical example. For design point code validation, the cycle efficiencies calculated from the employed model are compared to published data from three different studies [6,38,44], where the recuperator is also designed by specific effectiveness. The operation conditions used in the validation cases and corresponding efficiency differences are listed in Table 1 and the efficiency comparison is shown in Fig. 3(a).

For off-design code validation, the cycle efficiencies under several typical off-design conditions are examined with those results from Ref. [38], as shown in Table 2. For maintaining similar design parameters, the recuperators conductance used for design condition in Ref. [38] are converted to the recuperator effectiveness used in our model, and the results are also listed in Table 1. Since Dyreby *et al.* [38] did not introduce PHE and precooler into the power cycle, different TIT and CIT are used to represent the off-design conditions and the corresponding DPS inlet temperature and air inlet temperature used in our

models are shown in Table 2. As it is shown in Fig. 3(b), the calculated efficiencies are in close agreement with the published data, indicating that the modelling approach is consistent and reliable for the off-design performance analysis of the S-CO<sub>2</sub> Brayton cycle.

4. Performance analysis

4.1. System performance comparison at design points

This section introduces the design point specifications of different configurations under the same boundary conditions. Main design specifications are listed in Table 3. Besides these physical boundaries, technical features like the recompression fraction (RF), intermediate pressure of precompression and split expansion also significantly influence the cycle performance. Thus, a genetic algorithm [45] is utilized in the design condition to obtain the optimal operating conditions for the maximum cycle efficiency. The optimized parameters and their corresponding values in each cycle are listed in Table 4.

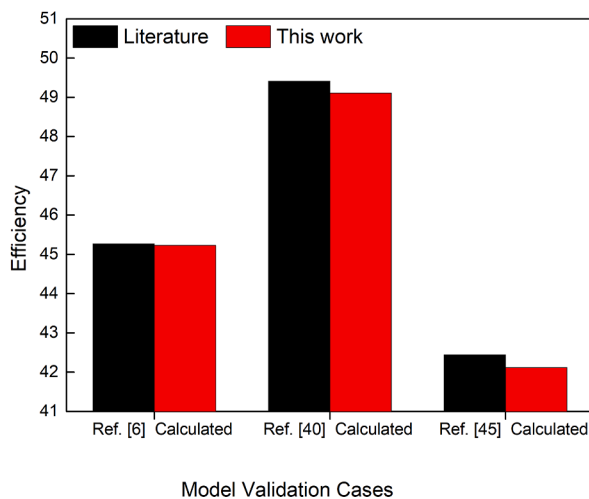
The system performance for these six cycles under their optimal design conditions are listed in Table 5. It can be seen that the intercooling cycle presents the highest cycle efficiency (52.11%), followed by recompression cycle, split expansion cycle and intercooling cycle. The partial cooling system has the largest specific work (141.91 J/kg) and

**Table 2**  
Operating conditions used for the off-design model validation. (Cycle layout: Recompression cycle).

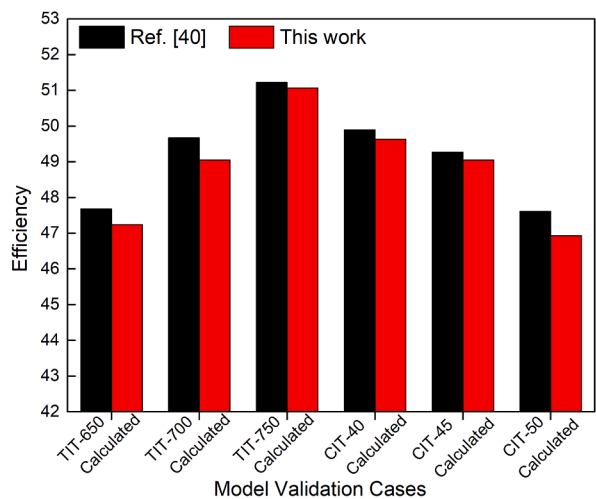
Parameter	Turbine Inlet Temperature			Compressor Inlet Temperature		
	650 °C	700 °C <sup>b</sup>	750 °C	40 °C	45 °C <sup>b</sup>	50 °C
DPS inlet temperature (T <sub>DPS</sub> ) (°C) <sup>a</sup>	670.39	720	769.48	719.75	720	721.71
Air inlet temperature (T <sub>air</sub> ) (°C) <sup>a</sup>	24.61	25	25.36	5	25	36.81
Percentage error reference vs calculated (%)	0.92	1.24	0.31	0.52	0.44	1.42

<sup>a</sup> The DPS inlet temperature and air inlet temperature are corresponding parameters used in our developed model which can generate the same turbine inlet temperature and compressor inlet temperature in Ref. [38].

<sup>b</sup> Values used in design condition.



(a) Efficiency comparisons at design condition



(b) Efficiency comparisons at off-design condition

Fig. 3. Efficiency comparisons for model validation at design (left) and off-design (right) conditions presented in Tables 2 and 3.

**Table 3**  
Fixed design boundaries and component efficiencies used for these six cycles.

Fixed parameters	Value	Note
Net electrical power (MW)	10	Representative system capacity considered by NREL for using in CSP [38]
Minimum cycle pressure (MPa)	7.8	Near the critical pressure of CO <sub>2</sub> [21]
Maximum cycle pressure (MPa)	25	Available and economic piping [21]
Air inlet temperature (°C)	20	Recommended design air temperature for direct dry cooling [46–48]
CIT (T1) (°C)	40	Possible under dry cooling with 20 °C temperature difference with air inlet temperature [46–48] T11 = T1 in intercooling cycle; T10 = T1 in partial cooling
DPS inlet temperature (°C)	700	Recommended inlet DPS design temperature in Ref. [21]
TIT (°C)	680	20 °C difference with DPS inlet temperature [21]
Turbine efficiency (%)	93	Projection of mature, commercial size radial flow turbine efficiency [49]
Compressor efficiency (%)	89	Lab test result [43]
PCHE recuperator efficiency (%)	95	The common value reported in the literature [6,20,30]

**Table 4**  
Optimized operation parameters for maximum cycle efficiency in each system configuration.

Parameters	Optimized values	Note
Recompression fraction (–)	0.25 for recompression and split expansion cycle 0.32 for intercooling cycle 0.35 for partial cooling cycle	The ratio of mass flow rate going through recompressor to the whole system mass flow rate
Intermediate pressure for split expansion (MPa)	20	The outlet pressure of split turbine in split expansion cycle
Intermediate pressure for precompression (MPa)	9.9 for partial cooling cycle 10.5 for precompression cycle 9.1 for intercooling cycle	The outlet pressure of precompressor in precompression, intercooling and partial cooling cycle

**Table 5**  
Comparison of six cycle performances under their optimal design conditions.

Configuration	Cycle efficiency (%)	Specific work (kJ/kg)	The temperature difference of DPS in PHE (°C)
Simple regeneration	43.63	131.04	216.62
Recompression	50.00	116.60	158.71
Precompression	48.56	132.91	196.92
Intercooling	52.11	130.67	174.28
Partial Cooling	49.46	141.91	205.26
Split Expansion	49.54	115.26	160.26

the split expansion cycle leads to the lowest specific work. In terms of the thermal ability of integration with TES, both the temperature differences of DPS in PHE in simple regeneration cycle and partial cooling cycle are larger than 200 °C, while the DPS temperature difference in recompression cycle is only 158.71 °C. The performance of split expansion cycle is similar to the recompression cycle. Compared to recompression cycle, the intercooling cycle contributes to better performance in terms of all these three aspects, while the partial cooling cycle presents less cycle efficiency. It is pointed out that introducing intercooling with multistage main compression is beneficial to increase the specific work

and DPS temperature difference, but not always good for the cycle efficiency.

Table 6 presents the geometric design specifications of each component at the design point. As seen in the first part of Table 6, the conductance of PHE in the simple regeneration system is significantly larger than those in the other five cycles. This is because being derived from simple regeneration cycle, the other five cycles have higher temperature in the PHE at the inlet of HTR and LTR. Compared with the other five cycles, the precompression cycle requires much larger pre-cooler but smaller PCHE recuperators. The size of the whole recuperators in the intercooling cycle and partial cooling cycle is similar, while the intercooling cycle requires smaller PHE and pre-cooler than the partial cooling cycle. Split expansion cycle always contributes to more complex system configurations, though less system performance improvement as compared to recompression cycle. The design point values of the turbomachinery for these six cycles are shown in the third part of Table 6.

#### 4.2. Off-design performance comparison under varying DPS inlet temperature

The DPS temperature at the inlet of PHE ( $T_{DPS}$ ) is a potential control parameter to provide a dispatchable power output following the power demand. The power cycle might operate at different  $T_{DPS}$  according to the operation and control or turbine dispatch strategies adopted or due to lower outlet temperatures at the exit of the solar receiver during on-sun operation. This section compares the off-design performance of different configurations at  $T_{DPS}$  varying from 460 °C to 700 °C (design value). The mass flow rate of DPS, inlet temperature and mass flow rate of air in the dry cooler, and operation parameters, including main shaft speed, RF and turbine outlet pressure, are all held constant at their design-point values.

Fig. 4 plots the  $W_{net}$  of all configurations under different  $T_{DPS}$ . As expected, when  $T_{DPS}$  decreases from its design value (700 °C),  $W_{net}$  decreases in every configuration, and the precompression cycle yields the highest off-design  $W_{net}$ , followed by the partial-cooling cycle, simple regeneration cycle, intercooling cycle and recompression cycle. The  $W_{net}$  in the split expansion cycle is similar to that in the recompression cycle. To further explain the  $W_{net}$  variations, the turbine power output ( $W_t$ ) and compressor work consumption ( $W_c$ ) at two typical  $T_{DPS}$  cases of 460 °C and 700 °C for six configurations are compared in Table 7. For each configuration,  $W_t$  decreases but  $W_c$  increases with the decreases of  $T_{DPS}$ . The reduction in  $W_t$  is the main cause of the decrease in  $W_{net}$ , as the numerical order of  $W_t$  reduction in six configurations is the same as the numerical order of  $W_{net}$  shown in Fig. 4. The precompression cycle performs with the largest increment of  $W_c$ , but the smallest reduction in  $W_t$ , and subsequently the smallest reduction in  $W_{net}$ . The recompression cycle and split expansion cycle have the largest reduction in  $W_t$  and thus the lowest  $W_{net}$ . Due to the lower  $W_c$  increment, the partial cooling cycle has a little bit higher  $W_{net}$  than that of the simple regeneration cycle, although it has higher  $W_t$  reduction.

The turbomachinery off-design behaviour ( $W_t$  and  $W_c$ ) depends on inlet conditions of the working fluid, rotation speed and performance map. Fig. 5 depicts the variations of CO<sub>2</sub> working conditions at the turbomachinery inlet, i.e., mass flow rate, TIT and turbine inlet pressure (TIP), main compressor inlet temperature (MCIT) and pressure (MCIP), and the precompressor inlet temperature (PCIT). From Fig. 5 (a), it could be seen that the mass flow rate of CO<sub>2</sub> in each configuration exhibits a linear increase with the decrease of  $T_{DPS}$ . This is because the allowable cycle off-design mass flow rate depends on the CO<sub>2</sub> density at the turbine outlet, as shown in Eq. (10). As the compressor inlet pressure remains constant with its design value, the turbine outlet pressure is almost the same value (with only slight changes because of the pressure drop in heat exchangers). Thus the CO<sub>2</sub> density at the turbine outlet only depends on the turbine outlet temperature which presents a similar variation trend to TIT. At high pressures in the supercritical region, the CO<sub>2</sub>

**Table 6**  
Components geometry designs for six S-CO<sub>2</sub> Brayton cycle configurations.

	Simple regeneration	Recompression	Precompression	Intercooling	Partial Cooling	Split Expansion
Part 1 – PHE and precooler design						
PHE UA (kW/K)	782.57	644.08	706.07	629.69	683.93	653.23
DPS mass flow rate (kg/s)	91.99	109.57	92.85	95.83	85.64	109.53
Precooler UA (kW/K)	378.97	271.21	621.72	194.06(PRC)	286.67(PRC)	319.057
				280.23(IRC)	279.29(PAC)	
Air mass flow rate (kg/s)	276.41	336.23	346.86	197.34(PRC) 209.87(IRC)	167.98(PRC)	225.32
					229.22(PAC)	
Part 2 – PCHE recuperators design						
HTR UA (kW/K)	592.55	1063.94	676.18	829.81	589.41	1099.89
HTR Volume(m <sup>3</sup> )	0.63	1.02	0.72	0.86	0.66	1.04
LTR UA (kW/K)	–	1202.19	832.87	1006.91	1111.17	1179.07
LTR Volume(m <sup>3</sup> )	–	1.3334	0.7729	1.1767	1.3108	1.2986
Part 3 – Turbomachinery design						
Main Comp. Diameter (m)	0.179	0.164	0.136	0.120	0.107	0.165
RC Comp. Diameter (m)	–	0.118	0.334	0.119(RC) 0.258(PC)	0.098(RC)0.268(PC)	0.119
Turbine Diameter (m)	0.252	0.231	0.286	0.222	0.215	0.210
						0.049 (ST)
Effective nozzle Area (m <sup>2</sup> )	0.0024	0.0027	0.0024	0.0024	0.0022	0.0031
						0.0024 (ST)
Turbine mass flow rate (kg/s)	76.32	85.76	75.88	76.53	70.47	86.76
Main Comp. Shaft speed (rpm)	33,494	36,485	29,549	38,053	39,182	36,274
RC Comp. speed (rpm)	–	71,856	13,117 (PC)	64,432(RC)	55,671 (RC)	71,494
				7592 (PC)	9129 (PC)	

Note: PRC refers to the precooler; IRC refers to the intercooler; PAC refers to the partial cooler; RC refers to the recompressor; PC refers to the precompressor; Main Comp. refers to the main compressor; RC Comp. refers to the second or third compressor; ST refers to the split turbine.

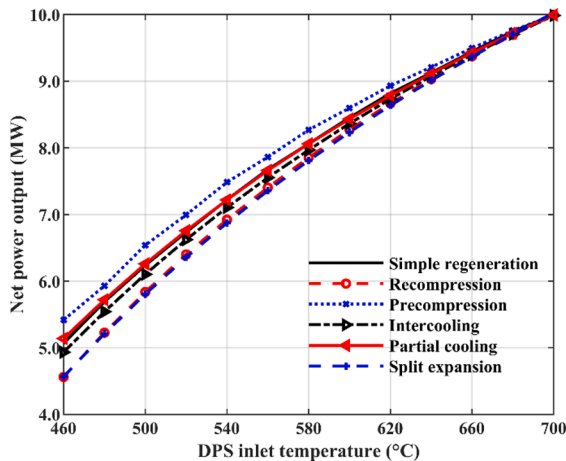


Fig. 4. Variation of  $W_{net}$  in six configurations with  $T_{DPS}$ .

density varies almost linearly with temperature. Therefore, when TIP decreases linearly with  $T_{DPS}$ , as shown in Fig. 5(b), the CO<sub>2</sub> density increases linearly resulting in a linear increase in mass flow rate. For these six configurations, the cycle mass flow rate changes 13.61%, 13.23%, 17.25%, 11.86%, 11.08% and 11.81% from their design values respectively.

The variation of mass flow rate changes the energy equilibrium in compressors and heat exchangers and makes them working in off-design conditions. The augmented mass flow rate of CO<sub>2</sub> leads to a lower main compressor outlet pressure (MCOP) due to the constant rotor speed. Meanwhile, the increased CO<sub>2</sub> density leads to an increase in CO<sub>2</sub> viscosity, so the pressure drops in heat exchangers also increase. The decreased MCOP and increased pressure drop make TIP decreasing with  $T_{DPS}$  reduction as shown in Fig. 5(c). On the other hand, the augmented mass flow rate of CO<sub>2</sub> also means that more mass of CO<sub>2</sub> needed to be cooled by the same ambient temperature and mass flow rate, leading to an increment in MCIT shown in Fig. 5(d). Among all configurations, the precompression cycle has the most significant variation in S-CO<sub>2</sub> mass flow rate, leading to the largest change in its MCIT.

TIP is the most important parameter affecting  $W_t$ , as it determines the turbine pressure ratio. With a low  $T_{DPS}$ , the precompression cycle has the highest TIP, which means it has the highest MCOP. The MCOP not only

**Table 7**  
Power output comparison of different configurations in  $T_{DPS} = 460\text{ °C}$  and  $700\text{ °C}$  (design point).

Power (MW)	Simple regeneration	Recompression	Precompression	Intercooling	Partial cooling	Split expansion
$W_{net, 700\text{ °C}}$	10	10	10	10	10	10
$W_{net, 460\text{ °C}}$	5.07	4.56	5.42	4.93	5.14	4.57
$W_{net, reduction}$	4.93	5.44	4.58	5.07	4.86	5.43
$W_t, 700\text{ °C}$	13.85	15.43	13.77	13.84	12.76	15.53
$W_t, 460\text{ °C}$	9.15	10.21	9.59	8.83	7.97	10.24
$W_t, reduction$	4.7	5.22	4.17	5.01	4.79	5.29
$W_t, reducing\ ratio$	0.34	0.34	0.3	0.36	0.38	0.34
$W_c, 700\text{ °C}$	3.86	5.44	3.78	3.85	2.77	5.5
$W_c, 460\text{ °C}$	4.09	5.65	4.18	3.89	2.83	5.67
$W_c, increment$	0.23	0.21	0.4	0.04	0.06	0.16
$W_c, increasing\ ratio$	0.06	0.04	0.11	0.01	0.02	0.03

Note:  $W_{net}$  refers to the cycle net power output;  $W_t$  refers to the turbine power output;  $W_c$  refers to the compressor power consumed in total;  $W_t, reduction$  and  $W_c, increment$  refer to the absolute value difference between the power under  $T_{DPS}$  of  $460\text{ °C}$  and the power under design point for turbine and compressor respectively;  $W_t, reducing\ ratio$  and  $W_c, increasing\ ratio$  refer to one minus the ratio of power under  $T_{DPS}$  of  $460\text{ °C}$  to the power under design point.

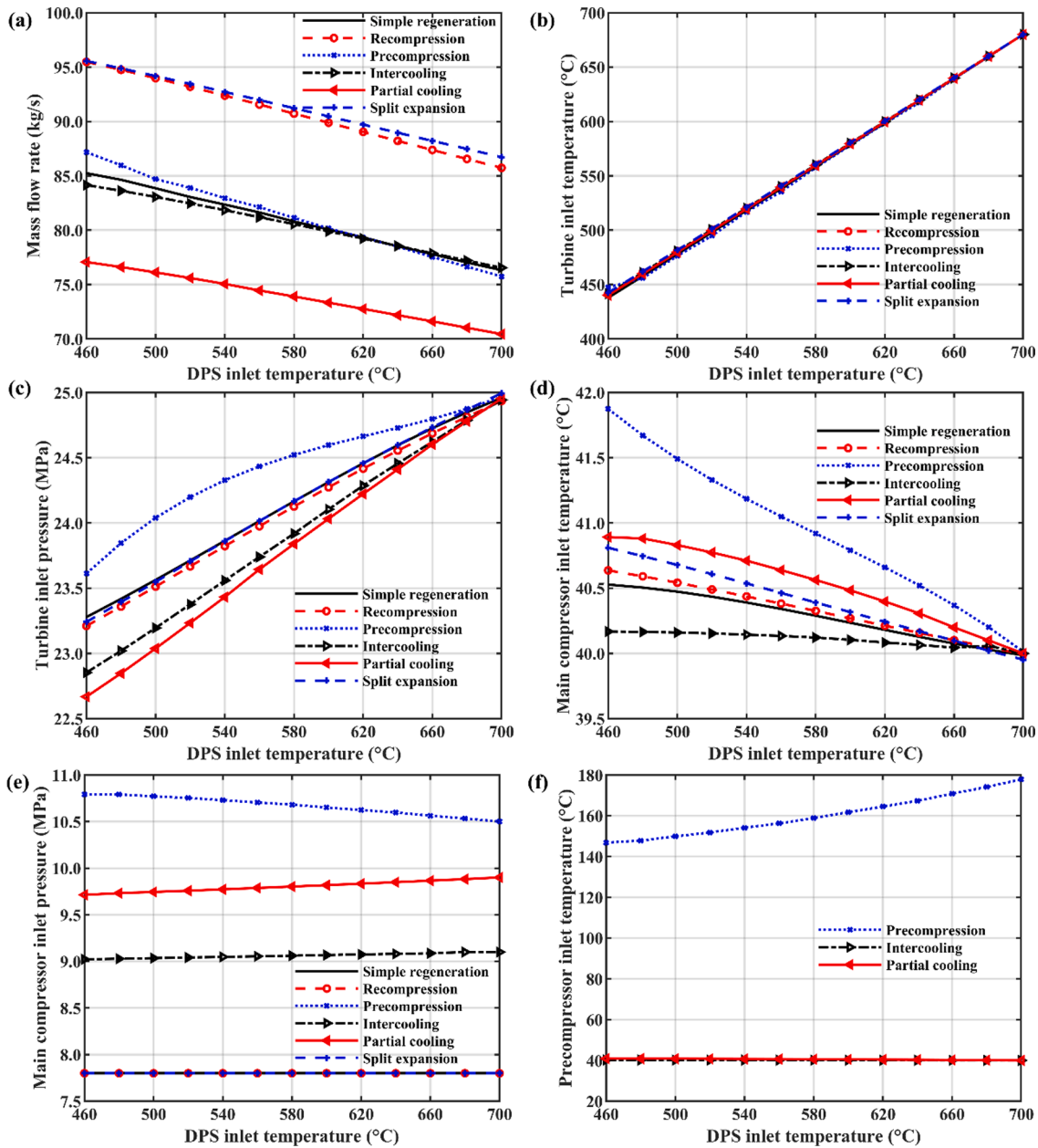


Fig. 5. Variations of system operation parameters with  $T_{DPS}$ .  $T_{DPS} = 700$  °C at design point. (a) Mass flow rate; (b) Turbine inlet temperature; (c) Turbine inlet pressure; (d) Main compressor inlet temperature; (e) Main compressor inlet pressure; (f) Precompressor inlet temperature.

relates to the mass flow rate but also MCIT as well as the main compressor inlet pressure (MCIP). As shown in Fig. 5(e), MCIP in the precompression cycle rises slightly as  $T_{DPS}$  diminishes, rather than decreasing slightly like in the intercooling and partial cooling cycles, or keeping design value like in the simple regeneration, recompression and split expansion cycle. The slightly higher MCIP in the precompression cycle results in the minimal reduction of MCOP (similar value to TIP) among the six configurations. Since the precompressor is located after the HTR in the precompression cycle, the precompressor inlet temperature (PCIT) drops significantly as the  $T_{DPS}$  decreases, as shown in Fig. 5 (f), leading to an increase in inlet fluid density, which causes the increase in precompressor outlet pressure (PCOP) (similar value to the MCIP).

It also can be observed, in Fig. 5(c), that the simple regeneration, recompression and split expansion cycle have similar TIP, while the intercooling cycle and partial cooling cycle have lower TIP than these three configurations. That is mainly because the design states of main

compressor inlet (point 1) in the intercooling cycle and partial cooling cycle are closer to the critical point of  $CO_2$  than those in the simple regeneration, recompression and split expansion cycles, as shown the T-s diagram for each configuration in Fig. 1(a)–(f). The closer the design state of point 1 is to the critical point of  $CO_2$ , the more sensitive the main compressor performance is to changes in intake conditions and therefore the lower MCOP. Compared with intercooling cycle, the lower MCOP of the partial cooling cycle is mainly originated by the slight decreasing of MCIP shown in Fig. 5(e).

The turbomachinery pressure ratio and corresponding efficiencies in six configurations are shown in Fig. 6. As depicted in Fig. 6(a), the decrease in turbine pressure ratio corresponds to the reduction of  $W_t$ . Note that the pressure ratio in the partial cooling cycle, as well as TIP, is the lowest among the configurations, but its  $W_t$  reduction is the second-lowest as presented in Table 7. Similarly, the recompression cycle has the third-highest turbine pressure ratio, while yields the highest  $W_t$  reduction at the same time. This indicates that the  $W_t$  reduction also

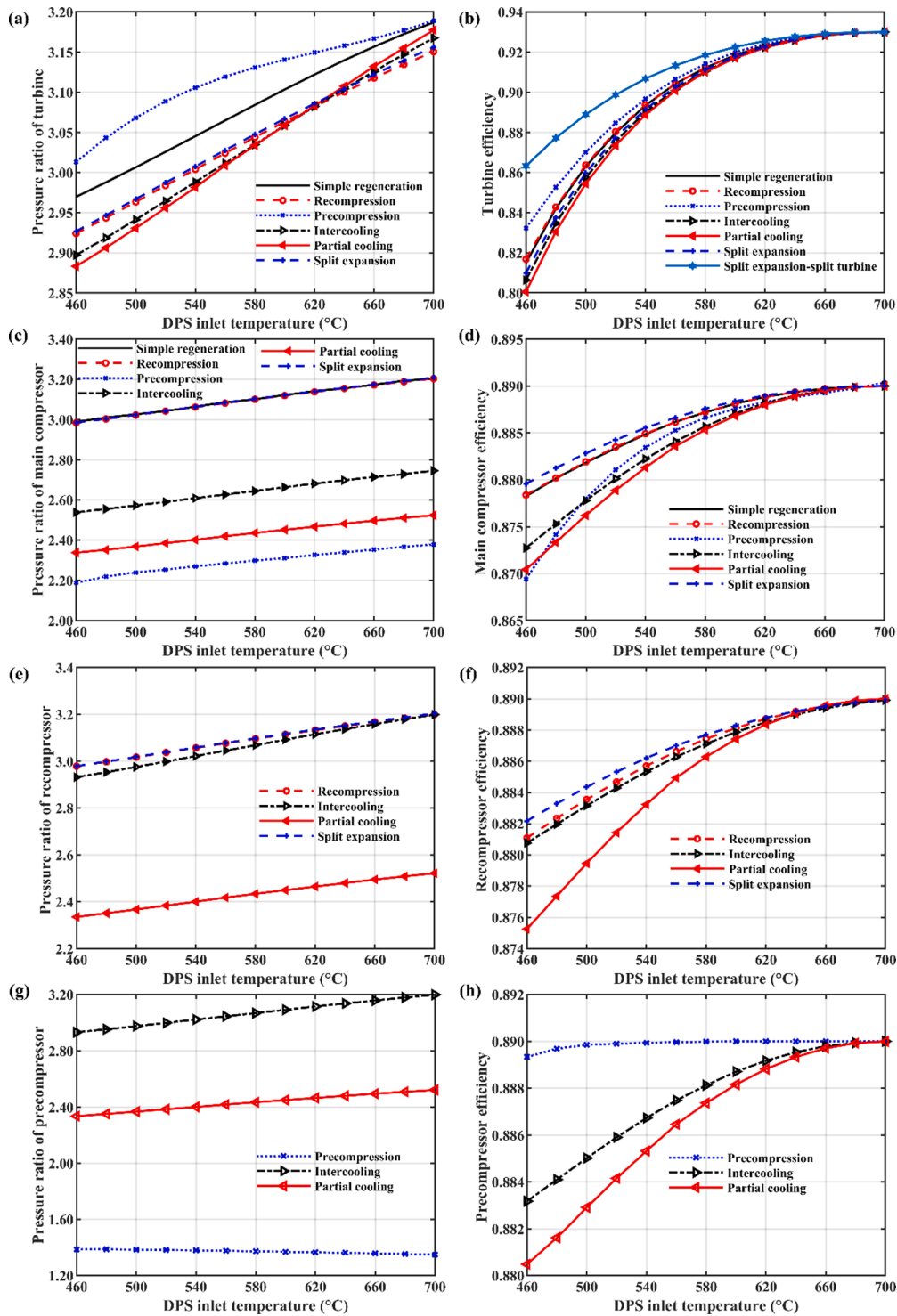


**Fig. 6.** Turbomachinery efficiencies versus  $T_{DPS}$  for six configurations. ( $T_{DPS} = 700\text{ }^{\circ}\text{C}$  at design point.) (a) Pressure ratio of the turbine; (b) Turbine efficiency; (c) Pressure ratio of the main compressor; (d) Main compressor efficiency; (e) Pressure ratio of recompressor; (f) Recompressor efficiency; (g) Pressure ratio of pre-compressor; and (h) Pre-compressor efficiency.

relates to the system specific work. A system with higher specific work not only has smaller components size but also lower  $W_{net}$  reduction under lower  $T_{DPS}$ . For all configurations, the compressor pressure ratio decreases with the reduction in  $T_{DPS}$  as shown in Fig. 6(e), (c) and (g).

In terms of turbomachinery efficiency shown in Fig. 6(b), (d), (f) and (h), it is obvious that the efficiency drop in the turbine is higher than that in compressor under the studied  $T_{DPS}$  range, as the fluid conditions changed more in the turbine inlet than the compressor inlet. This is also

one of the reasons that the  $W_t$  reductions for all configurations are higher than the corresponding  $W_c$  increments observed in Table 7. When the  $T_{DPS}$  is  $240\text{ }^{\circ}\text{C}$  lower than its design value, the biggest turbine efficiency drop is 13.98% (partial cooling cycle), while the biggest compressor efficiency drop is only 2.25% (main compressor of precompression cycle). The smaller efficiency drop observed in the split turbine is because the inlet temperature of the split expansion turbine is the outlet of HTR, and varies less than the outlet temperature of PHE. The smaller

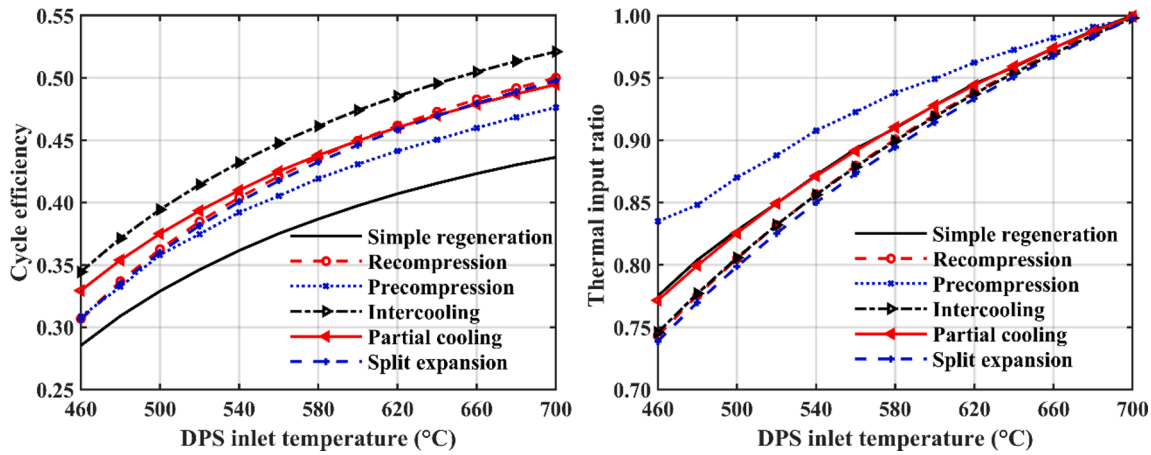


Fig. 7. (Left) Variation of cycle efficiency with  $T_{DPS}$ ; and (right) variation of the thermal input ratio with  $T_{DPS}$  in six S-CO<sub>2</sub> Brayton configurations.

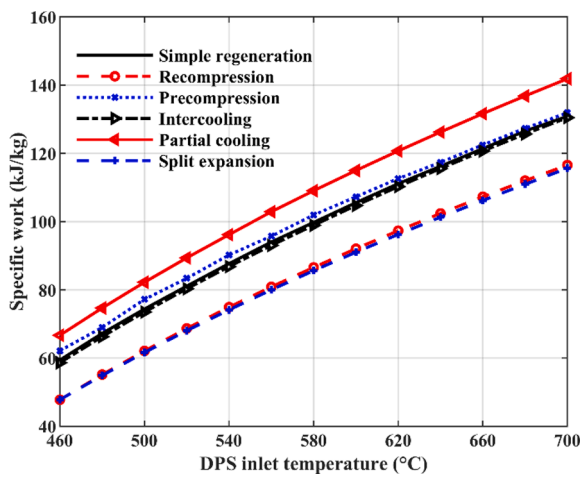


Fig. 8. Variation of specific work with  $T_{DPS}$  for six configurations.

the variation in the intake conditions of turbomachinery, the smaller the reduction in its efficiency.

Fig. 7 shows the effect of  $T_{DPS}$  on  $\eta_{cycle}$  and  $R_{thermal}$  for six configurations. Decreasing the  $T_{DPS}$  always contributes to a reduction in  $\eta_{cycle}$ . Under all cases, the intercooling system performs the highest  $\eta_{cycle}$ , while the simple regeneration system provides the lowest  $\eta_{cycle}$ . When the  $T_{DPS}$  drops 240 °C from its design value, the  $\eta_{cycle}$  of the simple regeneration, recompression, precompression, intercooling, partial cooling and split expansion cycle decreases 15.8%, 20.2%, 17.0%, 18.7%, 17.1% and 20.3% respectively. Compared to other configurations, the  $\eta_{cycle}$  of recompression and split expansion cycle is more sensitive to the  $T_{DPS}$  decreasing. In the design condition, the  $\eta_{cycle}$  of recompression cycle is higher than that of the partial cooling cycle and precompression cycle. However, if the  $T_{DPS}$  is lower than 600 °C, the  $\eta_{cycle}$  of the partial cooling cycle is higher than the recompression cycle; especially when the  $T_{DPS}$  equals to 460 °C, the precompression cycle has slightly higher  $\eta_{cycle}$  than the recompression and split expansion cycle. The  $\eta_{cycle}$  comparison among these configurations leads to similar results than those shown in Refs. [4,15]. That is because the TIT is nearly identical in all configurations and the temperature difference between TIT and  $T_{DPS}$  is near to the design value (20 °C), as shown in Fig. 5(b). Although similar TIT is found among all configurations,  $R_{thermal}$  is different due to the variation of mass flow rate and S-CO<sub>2</sub> inlet conditions of PHE. Although the  $W_{net}$  of precompression cycle drops less than other cycles, its high  $R_{thermal}$  reduces its attractiveness in terms of  $\eta_{cycle}$ . Conversely, the lower required  $R_{thermal}$  in intercooling system contributes to its highest  $\eta_{cycle}$  at a relative

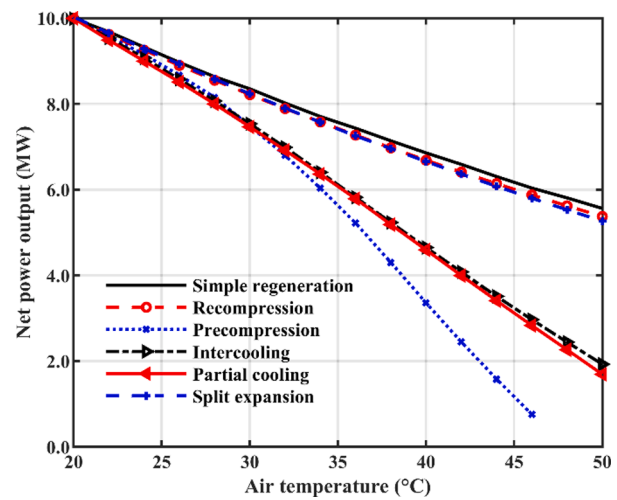


Fig. 9. Variation of  $W_{net}$  with  $T_{air}$  for six configurations. ( $T_{air} = 20$  °C at design point).

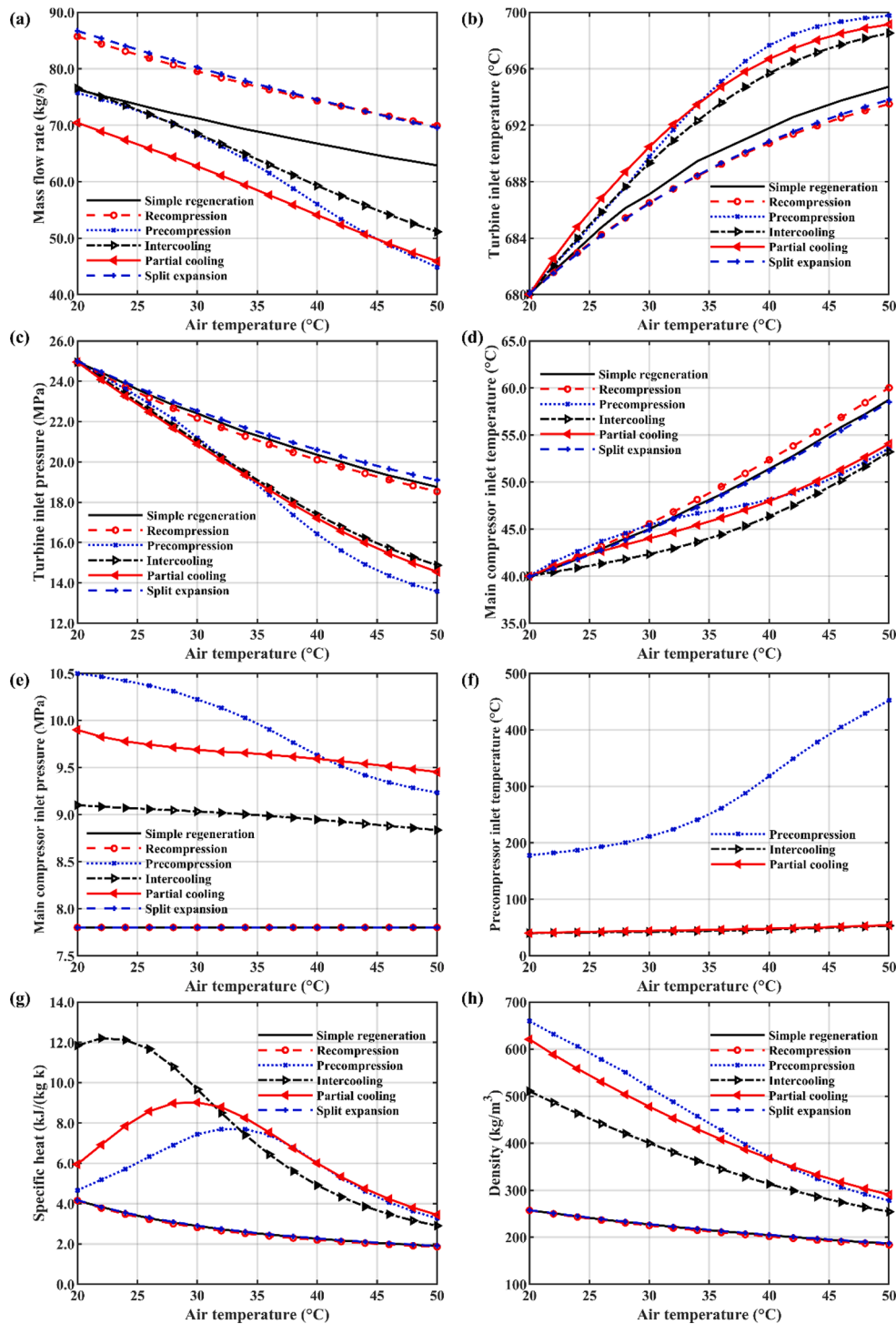
$W_{net}$ .

Fig. 8 shows the variation of specific work ( $w$ ) versus  $T_{DPS}$ . Decreasing the  $T_{DPS}$  from its design point,  $W_{net}$  diminishes and the cycle mass flow rate increases, thus  $w$  decreases for all configurations. The numerical order of  $w$  in the six configurations remains consistent with the order at design-point. At any  $T_{DPS}$  condition, the partial cooling cycle has the highest  $w$ , while the recompression and split expansion cooling cycle has the lowest  $w$ .

Overall, it can be seen that increasing the system complexity adds a bigger benefit to the  $\eta_{cycle}$  improvement than to the off-design  $W_{net}$  when the  $T_{DPS}$  decreases. Simple regeneration cycle provides higher  $W_{net}$  than the intercooling, recompression and split expansion cycles even though its  $\eta_{cycle}$  is the lowest. Although the intercooling cycle performs the highest  $\eta_{cycle}$ , its  $W_{net}$  is just higher than that of recompression and split expansion cycle. The configuration which contributes to the highest  $\eta_{cycles}$   $W_{net}$  and  $w$  at lower  $T_{DPS}$ , is the intercooling cycle, precompression cycle and partial cooling cycle, respectively.

#### 4.3. Off-design performance comparison under varying ambient temperature

This section compares the off-design performance of six configurations under different air temperature at the dry cooler inlet ( $T_{air}$ ). The investigated  $T_{air}$  varies from its design point (20 °C) to 50 °C, which is the probably highest ambient temperature in the sunny zones [50]. The



**Fig. 10.** Variation of system operation parameters with  $T_{air}$ . (a) Mass flow rate; (b) Turbine inlet temperature; (c) Turbine inlet pressure; (d) Main compressor inlet temperature; (e) Main compressor inlet pressure; (f) Precompressor inlet temperature; (g) Fluid Specific heat in the main compressor inlet; (h) Fluid density in the main compressor inlet.

other parameters are held in their design-point values, including the inlet conditions of DPS, the air mass flow rate, and cycle operation parameters (main shaft speed, RF and turbine outlet speed).

Fig. 9 illustrates the effect of  $T_{air}$  on  $W_{net}$ . As  $T_{air}$  increases, the linear decrease in  $W_{net}$  can be divided into two main categories:

the first category includes the simple regeneration, recompression, and split expansion cycles that exhibit similar net power output and the second category includes the precompression, intercooling, and partial cooling cycles that exhibit a greater decrease in net power output than

the first category.

In the first category, the simple regeneration cycle yields the highest  $W_{net}$  and it could provide more than 50% of the rated nominal power under extreme ambient temperature. The  $W_{net}$  of recompression and split expansion cycle is slightly lower than that of the simple regeneration. For the second category, the intercooling cycle performs very similarly to the partial cooling cycle in terms of  $W_{net}$ , both of which only provide about 20% of the rated nominal power at the hottest  $T_{air}$ .

It is noted the dramatic  $W_{net}$  drop in the precompression cycle when

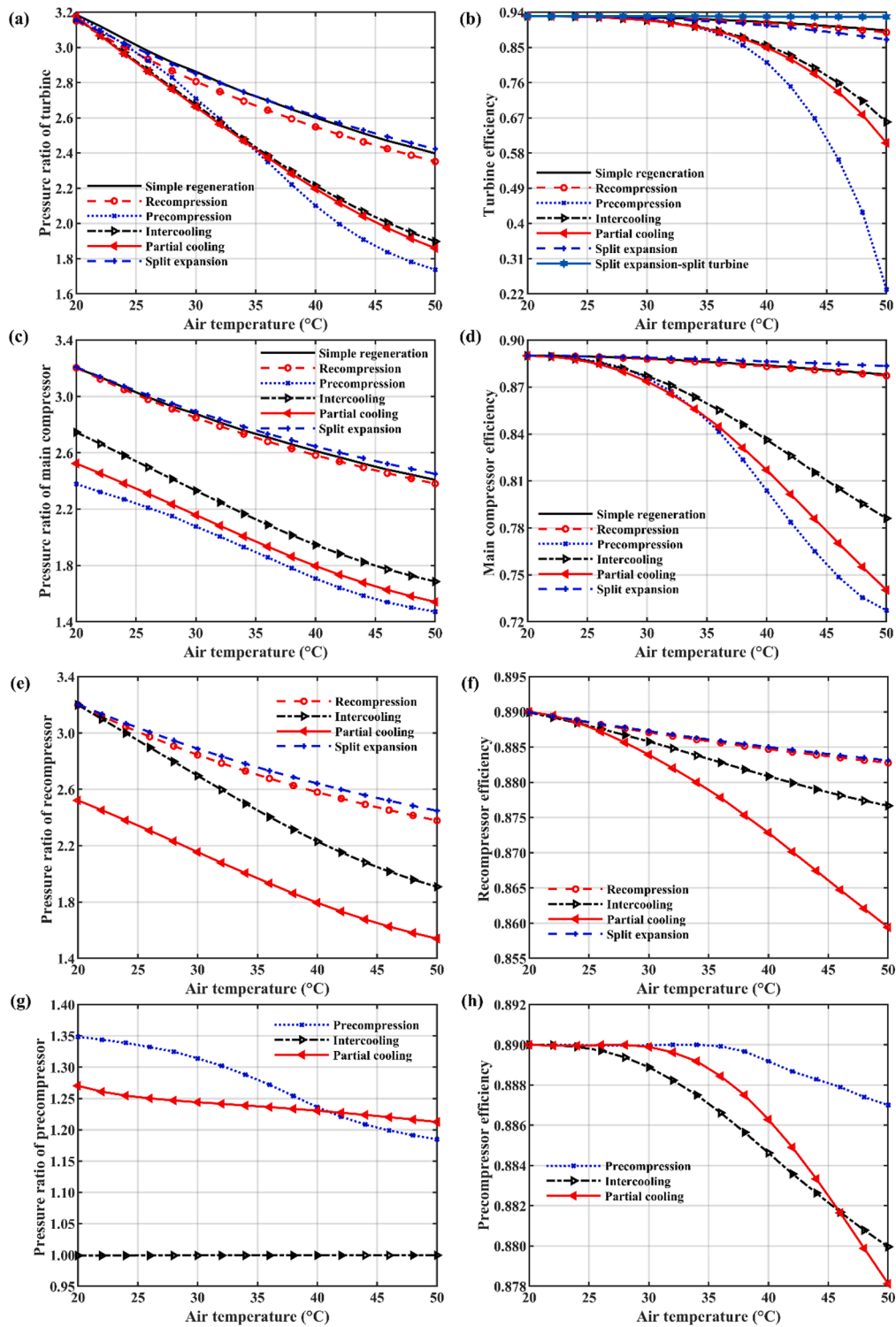


**Fig. 11.** Variation of turbomachinery pressure ratio and efficiencies with  $T_{air}$ . (a) Pressure ratio of the turbine; (b) Turbine efficiency; (c) Pressure ratio of the main compressor; (d) Main compressor efficiency; (e) Pressure ratio of the recompressor; (f) Recompressor efficiency; (g) Pressure ratio of the precompressor; and (h) Precompressor efficiency.

the  $T_{air}$  is higher than 32 °C. The precompression cycle only provides 7.56% of the rated nominal power at the  $T_{air}$  of 46 °C. Especially, when the  $T_{air}$  exceeds 46 °C, the cycle consumes more compression power than the expansion work, leading to a negative  $W_{net}$  and  $\eta_{cycles}$ , which are the unshown data of precompression cycle in Fig. 9. This is because the MCOP is too low to obtain enough pressure ratio for the turbine expansion work. The turbine efficiency also drops to <30%, as shown in

Fig. 11(b) so that  $W_t$  is lower than  $W_c$ . Therefore, the precompression cycle is limited to operate under high ambient temperature.

Fig. 10 presents the variation of plant operating parameters under different  $T_{air}$ . It can be seen that the variation of mass flow rate (Fig. 10(a)), TIT (Fig. 10(b)), TIP (Fig. 10(c)) and MCIT (Fig. 10(d)) has been depicted with the same classification of the two categories used for  $W_{net}$ . Resulting from matching the head-flow curve of the main compressor

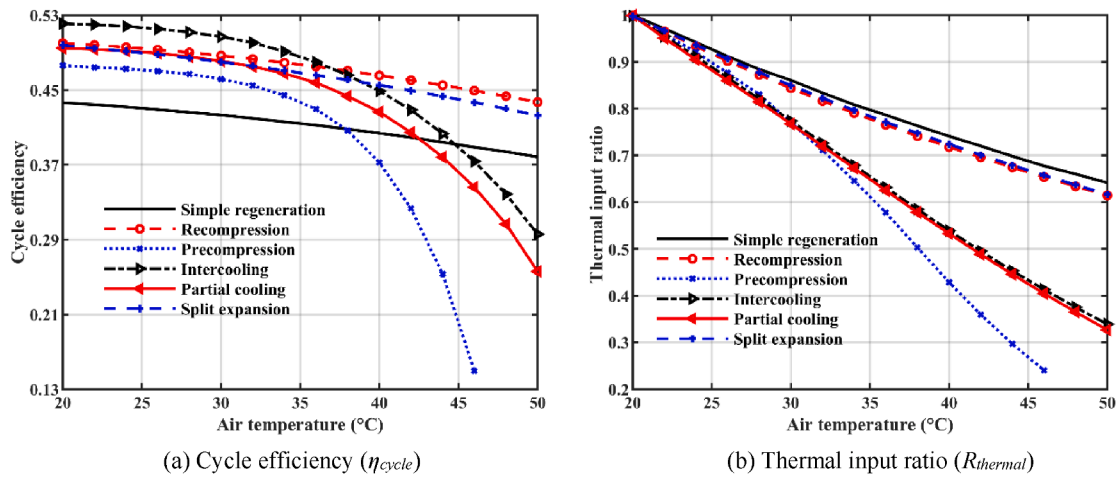


Fig. 12. (Left) Variation of the cycle efficiency and (right) variation of the thermal input ratio with  $T_{air}$  for six S- $CO_2$  Brayton configurations.

with the flow resistance of the turbine, a significant decrease in the mass flow rate of  $CO_2$  is obtained in each configuration. Both the increase of TIT shown in Fig. 10(b) and the decrease of TIP shown in Fig. 10(c) lead to a decrease of S- $CO_2$  density in the turbine inlet. As  $T_{air}$  increases, less S- $CO_2$  mass flow needs to be heated in the PHE, or cooled in the dry cooler, leading to a less temperature difference between S- $CO_2$  and DPS or air than its design value (20 °C). Due to the greater reduction in the mass flow rate, the precompression, intercooling and partial cooling cycle have a higher TIT than the other three configurations. As shown in Fig. 10(c), the variation of TIP resembles that of the net power output. As for MCIP shown in Fig. 10(e), it is noteworthy that MCIP of the precompression cycle drops from 10.5 MPa to 9.3 MPa, causing by an almost 180 °C increment of PCIT as shown in Fig. 10(f). The decrease of MCIP further contributes to a lower MCOP in precompression cycle, and therefore that cycle yields the lowest TIP.

Worth to note is that the precompression, intercooling and partial cooling cycles have less pronounced increments in MCIT than the simple regeneration, recompression and split expansion cycles, but a steeper decline in MCOP (same variation trend to TIP). This is because the design point of the main compressor inlet is nearer the critical region of  $CO_2$  in the precompression, intercooling and partial cooling cycles, where the fluid density and specific heat are highly variable. As shown in Fig. 10(g) and (h), changes in specific heat and density of the working fluid in the main compressor inlet change for the second configuration category are more significant than those for the first configuration category. Near the critical point, the density of  $CO_2$  has a strong decrease with increasing temperature, and this phenomenon is even more evident at low pressures. Due to the relatively large specific heat, the MCIT increments for the precompression, intercooling and partial cooling cycle are smaller than those for the other three configurations. The significant reduction in  $CO_2$  density accounts for the significant decrease in MCOP, contributing to a larger reduction in turbine pressure ratio and thus  $W_t$ . The more sensitive response to the main compressor inlet conditions makes these three systems performances drop more when  $T_{air}$  increases.

Fig. 11 shows the turbomachinery pressure ratios and efficiencies. These changes show the same classification of categories as  $W_{net}$ . When  $T_{air}$  increases, the machines, which includes precompression, intercooling and partial cooling cycles, show a more pronounced decrease in pressure ratio and efficiency than the machines in the first category. This is because they deviate from the design point on the performance map, due to the greater reduction in cycle mass flow rate. The lower pressure

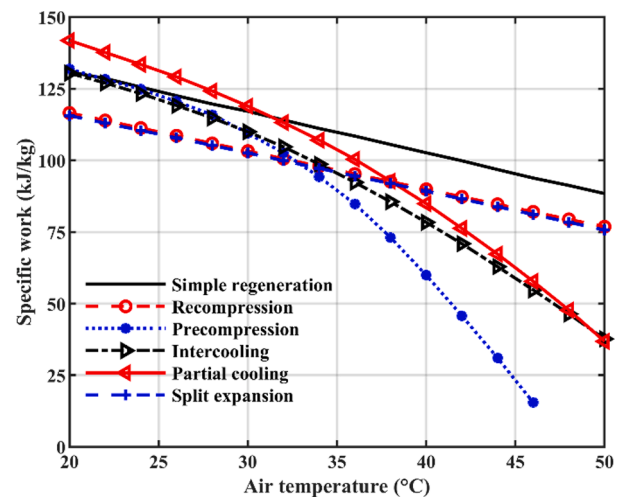


Fig. 13. Specific work versus air temperature for six S- $CO_2$  Brayton configurations.

ratios and efficiencies in the second configuration category result in a larger reduction in  $W_t$  and hence a lower  $W_{net}$  as shown in Fig. 9. When  $T_{air}$  is 50, the turbine and compressor efficiencies are reduced by only 6.45% and 1.12% in the first configuration category. However, for the second configuration category, the turbine efficiency decreases by 27.96% and 35.48% and the compressor efficiency decreases by 10.11% and 16.85% for the intercooling and partial cooling cycles, respectively. In particular, the precompression cycle has the largest reduction in efficiency for both the turbine (51.62%) and the main compressor (17.98%), resulting in the largest reduction in its  $W_{net}$  shown in Fig. 9. Due to the direct connection of the recompressor to the precompressor in the partial cooling cycle, its recompressor efficiency reduction is more significant than in other cycles.

Fig. 12 shows the variation of  $\eta_{cycle}$  and  $R_{thermal}$  with  $T_{air}$ . It can be seen that the  $\eta_{cycle}$  drops in simple regeneration, recompression and split expansion cycles are significantly less than in the precompression, intercooling and partial cooling cycles. From all the studied cases of  $T_{air}$ , the precompression cycle yields the highest  $\eta_{cycle}$  drop of 0.323, and the simple regeneration cycle provides the most stable  $\eta_{cycle}$ , which only

decreases 0.058. The intercooling cycle maintains the  $\eta_{cycle}$  advantage over other configurations for  $T_{air} < 38$  °C. Over that value, the recompression cycle is predicted to achieve the highest  $\eta_{cycle}$ , and when  $T_{air}$  exceeds 46 °C, the  $\eta_{cycle}$  of simple regeneration cycle becomes higher than that of intercooling, partial cooling and precompression cycle. At two  $T_{air}$  points of 38 °C and 46 °C, the decreasing rate of precompression cycle efficiency changes significantly, which corresponds to the obvious decrease in its turbine efficiency and precompressor efficiency as shown in Fig. 11(b) and (h). Even though the intercooling and partial cooling cycles seem to reach the US DOE's SunShot target of 50% efficiency at the design condition [3], their off-design performances, in terms of both  $\eta_{cycle}$  and  $W_{net}$ , decrease significantly when  $T_{air}$  is higher than 30 °C. This indicates that the simpler and recompression configurations reveal less sensitive to the changes in  $T_{air}$ .

The variations of specific work ( $w$ ) with  $T_{air}$  for all configurations are shown in Fig. 13. As  $T_{air}$  increases from its design value (20 °C),  $w$  always decreases, especially for the precompression cycle. Ordering the configurations by their  $w$ , it is observed that the order remains constant along with the entire range of  $T_{DPS}$  (see Fig. 8). However, variation with  $T_{air}$  shows that this order changes depending on the region of  $T_{air}$ . For  $T_{air}$  above 32 °C, the simple regeneration cycle takes over the highest  $w$ . When  $T_{air}$  is above 38 °C, the recompression cycle also starts to perform with higher  $w$  than the partial cooling cycle. At the  $T_{air}$  of 50 °C, the partial cooling and intercooling cycles have the same  $w$ .

Under all studied cases of varying  $T_{DPS}$  and  $T_{air}$ , the split expansion cycle always has coincident performance with the recompression cycle in terms of  $\eta_{cycle}$ ,  $W_{net}$  and  $w$ . Thus, the expansion splitting after HTR does not contribute to the improvement of system performance and operation stability, but only to the reduction of thermal stress in PHE [51].

For the integration with high-temperature CSP plants, usually located in sunny areas, it is expected a significant number of hours of operation above 30 °C ambient temperature, therefore simple regeneration and the recompression and split expansion cycles present better adaptation to that conditions.

## 5. Conclusions

In this study, a homogeneous comparative evaluation of both the design and off-design performance of six 10 MW S-CO<sub>2</sub> Brayton power cycle configurations has been carried out to assess the feasibility of S-CO<sub>2</sub> Brayton cycles application in DPS-based central receiver SPT plants with dry cooling systems. Detailed conclusions are as follows.

- 1) For the design condition, the intercooling system performs with the best cycle efficiency, followed by the recompression cycle, split expansion cycle, partial cooling cycle, precompression cycle and simple regeneration cycle. In terms of the specific work, the partial cooling system yields the highest specific work while the recompression layout offers the lowest specific work. Overall, if only the performance at design point is considered, as it is the case in a typical baseload SPT plant with many hours of thermal storage and operation 24/7, the intercooling cycle is the most recommended one due to its highest cycle efficiency, moderate specific work and good integration with the particle-based TES system (represented by the temperature difference of DPS in the hot side of PHE).
- 2) Under off-design conditions, produced by changes in temperature of the hot particles supplied by the solar receiver to the storage tank or by variations of ambient temperature, the variations of turbomachinery inlet conditions cause changes in cycle mass flow rate and

pressure ratio, which determine the cycle off-design net power output and thus its efficiency. Instead of heat exchangers, the cycle off-design performance mainly depends on the off-design characteristics of turbomachines.

- 3) Variations of  $T_{air}$  and its key role in the dry cooling system are leading to more significant impacts on cycle performance degradation than the reduction in  $T_{DPS}$ . When  $T_{DPS}$  is 240 °C less than the design value, most configurations could provide almost 50% of nominal power with about 30% cycle efficiency. However, the precompression cycle, which provides the highest net power output in lower  $T_{DPS}$ , could not generate positive power at the  $T_{air}$  higher than 46 °C.
- 4) Even though the complex systems present higher design-point cycle efficiency and specific work, such as intercooling and partial cooling cycles, their off-design performance exhibits a larger deterioration with increasing  $T_{air}$ . The closer the design-point fluid state at the inlet of the main compressor is to the critical point of CO<sub>2</sub>, the better the cycle design performance, but the more sensitive the cycle off-design performance is to the increase in  $T_{air}$ .
- 5) Off-design performance ranking of the six configurations changes depending on the regions of  $T_{DPS}$  and  $T_{air}$ . In the region of  $600$  °C <  $T_{DPS}$  <  $700$  °C, the recompression cycle has a higher cycle efficiency than the partial cooling cycle, while the trend reverses at  $T_{DPS}$  <  $600$  °C. When  $T_{air}$  is below 38 °C, the cycle efficiency of the intercooling cycle is greatest, whereas, the largest cycle efficiency is exhibited by the recompression cycle when  $T_{air}$  is above 38 °C. In the region of  $20$  °C <  $T_{air}$  <  $32$  °C, the partial cooling cycle presents the highest specific work, but for  $T_{air}$  >  $32$  °C, the simple regeneration exhibits the highest specific work.

In conclusion, selecting a suitable S-CO<sub>2</sub> configuration should simultaneously consider the system design and off-design performance, especially under typical off-design operating conditions. Thus, the simple regeneration and the recompression cycles might be the best selection of dry-cooled S-CO<sub>2</sub> Brayton cycle configuration to integrate with the CSP plants using DPS as both the HTF and TES medium particle. These two configurations present better adaptation (fewer performance degradations than other cycles) when  $T_{air}$  is above 30 °C, which is a condition expected in a significant number of hours every year in sunny areas. The disadvantage of low design cycle efficiency in simple regeneration cycle is balanced by its lower sensitiveness to the variation of  $T_{air}$  and fewer components requirement.

## CRedit authorship contribution statement

**Rui Chen:** Conceptualization, Methodology, Investigation, Software, Validation, Writing - original draft. **Manuel Romero:** Conceptualization, Investigation, Resources, Project administration, Writing - review & editing. **Jose González-Aguilar:** Conceptualization, Validation, Resources, Writing - review & editing. **Francesco Rovense:** Methodology, Investigation, Writing - review & editing. **Zhenghua Rao:** Conceptualization, Project administration. **Shengming Liao:** Supervision, Funding acquisition, Project administration.

## Declaration of Competing Interest

The authors declare that they have no known competing financial interests or personal relationships that could have appeared to influence the work reported in this paper.

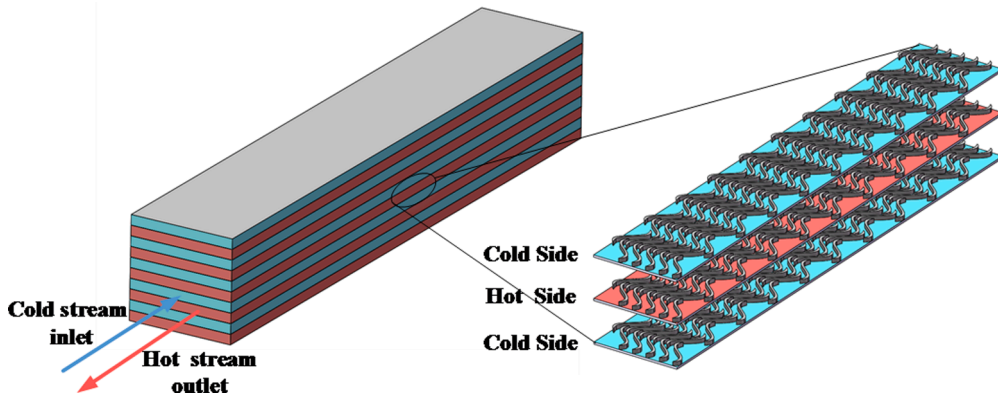


Fig. A1. The schematic geometry of an S-shaped fin PCHE.

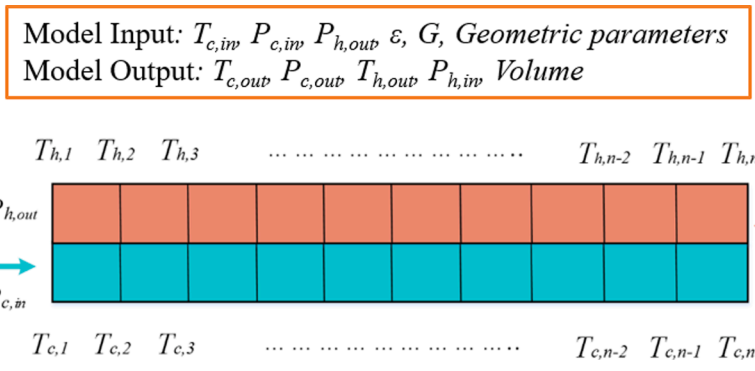


Fig. A2. The schematic sketch of the discretized PCHE counter-flow channel.

**Acknowledgements**

This work is supported by the Chinese Scholarship Council (No.201906370105), Graduate Independent Explorative Innovation Foundation of Central South University (No.502221703), and Hunan Provincial Natural Science Foundation of China (2020JJ4722). The

authors acknowledge the support from the European Union’s Horizon 2020 research and innovation programme under grant agreement No 727762, Next-CSP project. The authors wish to thank “Comunidad de Madrid” and European Structural Funds for their financial support to ACES2030-CM project (S2018/EMT-4319).

**Appendix A**

The detailed models of heat exchangers are described in this Annex. Fig. A1 shows the schematic geometry of the S-shaped fin PCHE. By adopting periodic boundary conditions, the recuperator can be modelled as a single counter-flow channel unit [36]. To consider the variations in thermophysical properties of S-CO<sub>2</sub>, the channel unit is further discretized into sufficient heat exchangers sections along the channel length, as shown in Fig. A2. The number of sub-heat exchangers depends on the extent of S-CO<sub>2</sub> thermophysical properties variability [6]. Outlet conditions on the hot side and cold side are estimated by knowing the inlet conditions on both sides and the desired value of recuperator effectiveness. Recuperator effectiveness ( $\varepsilon$ ) is defined as the ratio between the actual heat flow transferred to the maximum achievable heat flow transferred, as shown in Eq. (1).

$$\varepsilon = \frac{C_h(T_{h,in} - T_{h,out})}{C_{min}(T_{h,in} - T_{c,in})} \tag{1}$$

where  $C_h$  is the capacity rate of the hot stream,  $C_{min}$  is the minimum capacity rate of cold and hot streams, where the capacity rate is the product of the flow specific heat and the corresponding mass flow rate.  $T_{h, in}$  and  $T_{c, in}$  represent the inlet temperature of hot and cold stream respectively, and  $T_{h, out}$  is the outlet temperature of hot stream.

Enthalpy changes, in the whole recuperator, are estimated by assuming a pressure drop and, then, divided between each cell. After that, the pressure drop and heat transfer in each section are calculated from Eqs. (2)–(5). Once the assuming pressure drop is equal with the calculated one, the iteration in the recuperator model will end. The geometrical parameters used in pressure drop and heat transfer coefficient calculation are determined by the procedure explained in Ref. [36]. The length of the  $i$  element,  $\delta l_i$ , is calculated according to the equation;

$$\delta l_i = \frac{\delta \dot{Q}}{k_i \cdot \Delta T_i \cdot A_h} \tag{2}$$

where  $\delta\dot{Q}$  is the heat transfer rate in each division;  $\Delta T_i$  is the temperature difference between the hot and cold stream of the  $i$  element.  $A_h$  is the heat transfer area of the  $i$  element;  $k_i$  is the local overall heat transfer coefficient, and the  $Nu$  correlation used in the calculation of  $k_i$  is given by [35]:

$$Nu = 0.174 \cdot Re^{0.593} Pr^{0.43} \quad (3)$$

Once the length of recuperator is determined, the pressure drop at each side can be obtained by:

$$\Delta P = \sum_{i=1}^n \frac{f_i \cdot \rho u_i^2}{d} \cdot \delta l_i \quad (4)$$

where  $\rho$  is the fluid density,  $u$  is the fluid velocity,  $d$  is the hydraulic diameter and  $f$  is the friction factor given by Eq. (5) [35]:

$$f = 0.4545 \cdot Re^{-0.34} \quad (5)$$

The primary heat exchanger and precooler are modelled as a counter-flow configuration with a set of discrete sections. The model uses the inlet conditions of two streams and the desired temperature difference between the heat source (DPS or air) and S-CO<sub>2</sub>. The energy balance in the primary heat exchanger and precooler is presented as follows:

$$Q_{PHX} = m_{CO_2} \cdot (h_{CO_2,PHXout} - h_{CO_2,PHXin}) = m_{DPS} \cdot (h_{DPS,in} - h_{DPS,out}) \quad (6)$$

$$Q_{Pre} = m_{CO_2} \cdot (h_{CO_2,Prein} - h_{CO_2,Preout}) = m_{air} \cdot (h_{air,out} - h_{air,in}) \quad (7)$$

The pressure drops at the precooler and primary heat exchanger are calculated according to

$$\Delta p = \xi_p p_{in} \quad (8)$$

where  $\xi_p$  is the pressure-drop factor, assumed as 0.1% [21].

After calculating the heat exchanger performance with fixed effectiveness and fixed temperature difference, the conductance (UA) of these heat exchangers are further evaluated to compare the system complexity and characterize their off-design performance.

The conductance of heat exchanger can be obtained by the effectiveness-NTU method [52].

$$UA = \sum_{i=1}^n NTU_i \cdot C_{min} \quad (9)$$

$$NTU = \begin{cases} \frac{\log\left(\frac{1-\varepsilon \cdot C_R}{1-C_R}\right)}{1-C_R} & \text{if } C_R \neq 1 \\ \frac{\varepsilon}{1-\varepsilon} & \text{otherwise} \end{cases} \quad (10)$$

$$C_R = \frac{C_{min}}{C_{max}} \quad (11)$$

where  $NTU$  is the dimensionless number of transfer units for each division,  $C_{min}$  and  $C_{max}$  are the minimum capacitance rate and maximum capacitance rate of the hot and cold streams, respectively.

## References

- [1] Solar Power and Chemical Energy Systems. CSP Projects Around the World 2020. <https://www.solarpaces.org/csp-technologies/csp-projects-around-the-world/> (accessed October 1, 2020).
- [2] Romero M, González-Aguilar J. Solar thermal CSP technology. *Wiley Interdiscip Rev Energy Environ* 2014;3(1):42–59.
- [3] Mehos M, Turchi C, Vidal J, Wagner M, Ma Z, Ho C, et al. Concentrating Solar Power Gen3 Demonstration Roadmap. Nrel/Tp-5500-67464 2017:1–140. <https://doi.org/10.2172/1338899>.
- [4] Turchi CS, Ma Z, Neises T, Wagner M. Thermodynamic study of advanced supercritical carbon dioxide power cycles for high performance concentrating solar power systems. ASME 2012 6th Int. Conf. Energy Sustain. ES 2012, Collocated with ASME 2012 10th Int. Conf. Fuel Cell Sci. Eng. Technol., vol. July 23–26, 2012, p. 375–83. <https://doi.org/10.1115/ES2012-91179>.
- [5] Brun K, Friedman P, Dennis R. Fundamentals and applications of supercritical carbon dioxide (SCO<sub>2</sub>). *Based Power Cycles* 2017.
- [6] Dostal V, Driscoll MJ, Hejzlar P. A supercritical carbon dioxide cycle for next generation nuclear reactors. Tech Rep MIT-ANP-TR-100 2004:1–317.
- [7] Feher EG. The supercritical thermodynamic power cycle. *Energy Convers* 1968;8(2):85–90. [https://doi.org/10.1016/0013-7480\(68\)90105-8](https://doi.org/10.1016/0013-7480(68)90105-8).
- [8] Dunham MT, Iverson BD. High-efficiency thermodynamic power cycles for concentrated solar power systems. *Renew Sustain Energy Rev* 2014;30:758–70.
- [9] Ruiz-Casanova E, Rubio-Maya C, Pacheco-Ibarra JJ, Ambriz-Díaz VM, Romero CE, Wang X. Thermodynamic analysis and optimization of supercritical carbon dioxide Brayton cycles for use with low-grade geothermal heat sources. *Energy Convers Manag* 2020;216:112978. <https://doi.org/10.1016/j.enconman.2020.112978>.
- [10] Guo JQ, Li MJ, Xu JL, Yan JJ, Ma T. Energy, exergy and economic (3E) evaluation and conceptual design of the 1000 MW coal-fired power plants integrated with S-CO<sub>2</sub> Brayton cycles. *Energy Convers Manag* 2020;211:112713. <https://doi.org/10.1016/j.enconman.2020.112713>.
- [11] Liu Z, Liu B, Guo J, Xin X, Yang X. Conventional and advanced exergy analysis of a novel transcritical compressed carbon dioxide energy storage system. *Energy Convers Manag* 2019;198:111807. <https://doi.org/10.1016/j.enconman.2019.111807>.
- [12] Crespi F, Gavagnin G, Sánchez D, Martínez GS. Supercritical carbon dioxide cycles for power generation: A review. *Appl Energy* 2017;195:152–83. <https://doi.org/10.1016/j.apenergy.2017.02.048>.
- [13] Crespi F, Sánchez D, Rodríguez JM, Gavagnin G. A thermo-economic methodology to select sCO<sub>2</sub> power cycles for CSP applications. *Renew Energy* 2020;147:2905–12. <https://doi.org/10.1016/j.renene.2018.08.023>.
- [14] Al-Sulaiman FA, Atif M. Performance comparison of different supercritical carbon dioxide Brayton cycles integrated with a solar power tower. *Energy* 2015;82:61–71. <https://doi.org/10.1016/j.energy.2014.12.070>.
- [15] Zhu HH, Wang K, He YL. Thermodynamic analysis and comparison for different direct-heated supercritical CO<sub>2</sub> Brayton cycles integrated into a solar thermal power tower system. *Energy* 2017;140:144–57. <https://doi.org/10.1016/j.energy.2017.08.067>.
- [16] Iverson BD, Conboy TM, Pasch JJ, Kruijenga AM. Supercritical CO<sub>2</sub> Brayton cycles for solar-thermal energy. *Appl Energy* 2013;111:957–70. <https://doi.org/10.1016/j.apenergy.2013.06.020>.
- [17] Wang K, He YL, Zhu HH. Integration between supercritical CO<sub>2</sub> Brayton cycles and molten salt solar power towers: A review and a comprehensive comparison of different cycle layouts. *Appl Energy* 2017;195:819–36. <https://doi.org/10.1016/j.apenergy.2017.03.099>.
- [18] Wang K, Li M-J, Guo J-Q, Li P, Liu Z-B. A systematic comparison of different S-CO<sub>2</sub> Brayton cycle layouts based on multi-objective optimization for applications in solar power tower plants. *Appl Energy* 2018;212:109–21. <https://doi.org/10.1016/j.apenergy.2017.12.031>.
- [19] Ma Y, Morozuk T, Liu M, Yan J, Liu J. Optimal integration of recompression supercritical CO<sub>2</sub> Brayton cycle with main compression intercooling in solar power tower system based on exergoeconomic approach. *Appl Energy* 2019;242:1134–54. <https://doi.org/10.1016/j.apenergy.2019.03.155>.

- [20] Neises T, Turchi C. Supercritical carbon dioxide power cycle design and configuration optimization to minimize leveled cost of energy of molten salt power towers operating at 650 °C. *Sol Energy* 2019;181:27–36. <https://doi.org/10.1016/j.solener.2019.01.078>.
- [21] Reyes-Belmonte MA, Sebastián A, Romero M, González-Aguilar J. Optimization of a recompression supercritical carbon dioxide cycle for an innovative central receiver solar power plant. *Energy* 2016;112:17–27. <https://doi.org/10.1016/j.energy.2016.06.013>.
- [22] Reyes-Belmonte MA, Sebastián A, Spelling J, Romero M, González-Aguilar J. Annual performance of subcritical Rankine cycle coupled to an innovative particle receiver solar power plant. *Renew Energy* 2019;130:786–95. <https://doi.org/10.1016/j.renene.2018.06.109>.
- [23] Dyreby JJ, Klein SA, Nellis GF, Reindl DT. Modeling off-design and part-load performance of supercritical carbon dioxide power cycles. *Turbo Expo Power Land, Sea, Air*, vol. 55294, American Society of Mechanical Engineers; 2013, p. V008T34A014.
- [24] de la Calle A, Bayon A, Soo Too YC. Impact of ambient temperature on supercritical CO<sub>2</sub> recompression Brayton cycle in arid locations: Finding the optimal design conditions. *Energy* 2018;153:1016–27. <https://doi.org/10.1016/j.energy.2018.04.019>.
- [25] Duniam S, Veeraragavan A. Off-design performance of the supercritical carbon dioxide recompression Brayton cycle with NDDCT cooling for concentrating solar power. *Energy* 2019;187:115992. <https://doi.org/10.1016/j.energy.2019.115992>.
- [26] Singh R, Miller SA, Rowlands AS, Jacobs PA. Dynamic characteristics of a direct-heated supercritical carbon-dioxide Brayton cycle in a solar thermal power plant. *Energy* 2013;50:194–204. <https://doi.org/10.1016/j.energy.2012.11.029>.
- [27] Wang X, Li X, Li Q, Liu L, Liu C. Performance of a solar thermal power plant with direct air-cooled supercritical carbon dioxide Brayton cycle under off-design conditions. *Appl Energy* 2020;261:114359. <https://doi.org/10.1016/j.apenergy.2019.114359>.
- [28] Yang J, Yang Z, Duan Y. Off-design performance of a supercritical CO<sub>2</sub> Brayton cycle integrated with a solar power tower system. *Energy* 2020;201:117676. <https://doi.org/10.1016/j.energy.2020.117676>.
- [29] Yang J, Yang Z, Duan Y. Part-load performance analysis and comparison of supercritical CO<sub>2</sub> Brayton cycles. *Energy Convers Manag* 2020;214:112832. <https://doi.org/10.1016/j.enconman.2020.112832>.
- [30] Saeed M, Khatoun S, Kim MH. Design optimization and performance analysis of a supercritical carbon dioxide recompression Brayton cycle based on the detailed models of the cycle components. *Energy Convers Manag* 2019;196:242–60. <https://doi.org/10.1016/j.enconman.2019.05.110>.
- [31] Neises T. Steady-state off-design modeling of the supercritical carbon dioxide recompression cycle for concentrating solar power applications with two-tank sensible-heat storage. *To Appear Sol Energy* 2020;212:19–33. <https://doi.org/10.1016/j.solener.2020.10.041>.
- [32] Turchi CS, Ma Z, Dyreby J. Supercritical carbon dioxide power cycle configurations for use in concentrating solar power systems. *Turbo Expo Power Land, Sea, Air*, vol. 44717, American Society of Mechanical Engineers; 2012, p. 967–73.
- [33] *Mathworks I. MATLAB: R2014a*. Natick: Mathworks Inc; 2014.
- [34] Lemmon EW, Huber ML, McLinden MO. NIST Standard Reference Database 23: Reference Fluid Thermodynamic and Transport Properties-REFPROP, Version 8.0. National Institute of Standards and Technology. Standard Reference Data Program. Stand Ref Data Program, Gaithersburg 2018.
- [35] Ngo TL, Kato Y, Nikitin K, Ishizuka T. Heat transfer and pressure drop correlations of microchannel heat exchangers with S-shaped and zigzag fins for carbon dioxide cycles. *Exp Therm Fluid Sci* 2007;32(2):560–70. <https://doi.org/10.1016/j.expthermflusci.2007.06.006>.
- [36] Rao Z, Xue T, Huang K, Liao S. Multi-objective optimization of supercritical carbon dioxide recompression Brayton cycle considering printed circuit recuperator design. *Energy Convers Manag* 2019;201:112094. <https://doi.org/10.1016/j.enconman.2019.112094>.
- [37] Sienicki JJ, Moiseyev A, Fuller RL, Wright SA, Pickard PS. Scale dependencies of supercritical carbon dioxide Brayton cycle technologies and the optimal size for a next-step supercritical CO<sub>2</sub> cycle demonstration. *SCO<sub>2</sub> power cycle Symp.*, 2011.
- [38] Dyreby JJ, Klein SA, Nellis GF, Reindl DT. Modeling off-design and part-load performance of supercritical carbon dioxide power cycles. *Proc. ASME Turbo Expo* 2013;8:1–7. <https://doi.org/10.1115/GT2013-95824>.
- [39] Wright SA, Radel RF, Vernon ME, Rochau GE, Pickard PS. Operation and analysis of a supercritical CO<sub>2</sub> Brayton cycle. *Sandia Rep SAND2010-0171* 2010:1–101.
- [40] Dyreby JJ. Modeling the supercritical Carbon dioxide Brayton cycle with recompression. University of Wisconsin Madison; 2014.
- [41] Floyd J, Alpy N, Moiseyev A, Haubensack D, Rodriguez G, Sienicki J, et al. A numerical investigation of the sCO<sub>2</sub> recompression cycle off-design behaviour, coupled to a sodium cooled fast reactor, for seasonal variation in the heat sink temperature. *Nucl Eng Des* 2013;260:78–92. <https://doi.org/10.1016/j.nucengdes.2013.03.024>.
- [42] Chen H, Baines NC. The aerodynamic loading of radial and mixed-flow turbines. *Int J Mech Sci* 1994;36(1):63–79.
- [43] Wright SA, Radel RF, Vernon ME, Rochau GE, Pickard PS. Operation and Analysis of a Supercritical CO<sub>2</sub> Brayton Cycle 2010.
- [44] Ishiyama S, Muto Y, Kato Y, Nishio S, Hayashi T, Nomoto Y. Study of steam, helium and supercritical CO<sub>2</sub> turbine power generations in prototype fusion power reactor. *Prog Nucl Energy* 2008;50(2-6):325–32. <https://doi.org/10.1016/j.pnucene.2007.11.078>.
- [45] Whitley D. Genetic algorithms and evolutionary computing. *Van Nostrand's Sci Encycl* 2002.
- [46] Monjurul Ehsan M, Guan Z, Klimenko AY, Wang X. Design and comparison of direct and indirect cooling system for 25 MW solar power plant operated with supercritical CO<sub>2</sub> cycle. *Energy Convers Manag* 2018;168:611–28. <https://doi.org/10.1016/j.enconman.2018.04.072>.
- [47] Ehsan MM, Duniam S, Guan Z, Gurgenci H, Klimenko A. Seasonal variation on the performance of the dry cooled supercritical CO<sub>2</sub> recompression cycle. *Energy Convers Manag* 2019;197:111865. <https://doi.org/10.1016/j.enconman.2019.111865>.
- [48] Monjurul Ehsan M, Guan Z, Gurgenci H, Klimenko A. Novel design measures for optimizing the yearlong performance of a concentrating solar thermal power plant using thermal storage and a dry-cooled supercritical CO<sub>2</sub> power block. *Energy Convers Manag* 2020;216:112980. <https://doi.org/10.1016/j.enconman.2020.112980>.
- [49] Neises T, Turchi C. A comparison of supercritical carbon dioxide power cycle configurations with an emphasis on CSP applications. *Energy Procedia* 2014;49:1187–96. <https://doi.org/10.1016/j.egypro.2014.03.128>.
- [50] National Renewable Energy Laboratory (NREL). Weather Data - System Advisor Model (SAM). SAM 2020. <https://sam.nrel.gov/weather-data> (accessed December 15, 2020).
- [51] Rao Z, Bao S, Liu X, Taylor RA, Liao S. Estimating allowable energy flux density for the supercritical carbon dioxide solar receiver: A service life approach. *Appl Therm Eng* 2021;184:116054. <https://doi.org/10.1016/j.applthermaleng.2020.116054>.
- [52] Dyreby J, Klein S, Nellis G, Reindl D. Design considerations for supercritical carbon dioxide brayton cycles with recompression. *J Eng Gas Turbines Power* 2014;136. <https://doi.org/10.1115/1.4027936>.